GABRIEL CICELINI

NUMERICAL AND EXPERIMENTAL ANALYSIS OF THE FLOW OVER AN eVTOL CONCEPT

UNIVERSIDADE FEDERAL DE UBERLÂNDIA

FACULDADE DE ENGENHARIA MECÂNICA

2022

GABRIEL CICELINI

NUMERICAL AND EXPERIMENTAL ANALYSIS OF THE FLOW OVER AN eVTOL CONCEPT

Undergraduate thesis submitted to the Course of Aeronautical Engineering from the Federal University of Uberlândia as a part of requirement for obtaining the BACHELORS DEGREE ON AERONAUTICAL ENGINEERING.

Tutor: Prof. Dr. Odenir de Almeida

UBERLÂNDIA – MG

2022

UNIVERSIDADE FEDERAL DE UBERLÂNDIA
Coordenação do Curso de Graduação em Engenharia Aeronáutica
Rodovia BR 050, KM 78, Bloco 1D, 2º andar - Bairro Glória, Uberlândia-MG, CEP 38400-902
Telefone: (34) 2512-6768 - www.mecanica.ufu.br - coceaero@mecanica.ufu.br

ATA DE DEFESA - GRADUAÇÃO

Curso de Graduação em:	ENGENHARIA AERONÁUTICA				
Defesa de:	PROJETO DE CONCLUSÃO DE CURSO - FEMEC43100				
Data:	25/02/2022	Hora de início:	08:05	Hora de encerramento:	09:48
Matrícula do Discente:	11611EAR023				
Nome do Discente:	GABRIEL CICELINI				
Título do Trabalho:	Numerical and Experimental Analysis of the Flow Over an eVTOL Concept				

Reuniu-se remotamente, por meio da Plataforma Digital Microsof Teams, link de acesso do orientador, a Banca Examinadora designada pelo Colegiado do Curso de Graduação em Engenharia Aeronáutica, assim composta: Prof. Odenir de Almeida (FEMEC/UFU), orientador do candidato, Prof. Giuliano Gardolinski Venson (FEMEC/UFU) e Prof. Tobias Souza Morais (FEMEC/UFU).

Iniciando os trabalhos, o(a) presidente da mesa, Prof. Odenir de Almeida, apresentou a Comissão Examinadora e o candidato, agradeceu a presença do público, e concedeu ao discente a palavra, para a exposição do seu trabalho. A duração da apresentação do discente e o tempo de arguição e resposta foram conforme as normas do curso.

A seguir o(a) senhor(a) presidente concedeu a palavra, pela ordem sucessivamente, aos(às) examinadores(as), que passaram a arguir o(a) candidato(a). Ultimada a arguição, que se desenvolveu dentro dos termos regimentais, a Banca, em sessão secreta, atribuiu o resultado final, considerando o(a) candidato(a):

Aprovado, Nota: 90.

Nada mais havendo a tratar foram encerrados os trabalhos. Foi lavrada a presente ata que após lida e achada conforme foi assinada pela Banca Examinadora.

---

sei! assinatura eletrônica

Documento assinado eletronicamente por **Odenir de Almeida**, **Professor(a) do Magistério Superior**, em 25/02/2022, às 09:50, conforme horário oficial de Brasília, com fundamento no art. 6º, § 1º, do Decreto nº 8.539, de 8 de outubro de 2015.

Documento assinado eletronicamente por **Giuliano Gardolinski Venson**, **Professor(a) do Magistério Superior**, em 25/02/2022, às 09:50, conforme horário oficial de Brasília, com fundamento no art. 6º, § 1º, do Decreto nº 8.539, de 8 de outubro de 2015.

Documento assinado eletronicamente por **Tobias Souza Morais**, **Professor(a) do Magistério Superior**, em 25/02/2022, às 09:50, conforme horário oficial de Brasília, com fundamento no art. 6º, § 1º, do Decreto nº 8.539, de 8 de outubro de 2015.

A autenticidade deste documento pode ser conferida no site https://www.sei.ufu.br/sei/controlador_externo.php?acao=documento_conferir&id_orgao_acesso_externo=0, informando o código verificador **3402568** e o código CRC **09D6A678**.

ACKNOLEGEMENTS

First of all, I would like to dedicate this work to my parents, Fernando Antonio and Maria Cristina, for all the support they gave me since the very dawn of my life. Nothing of this would be possible without them, and for that I am deeply grateful.

Since the beginning of this project, I could count on my closest friends about every matter I needed advice on. These friendships are the most valuable gift I received during the engineering course, and for this reason I also dedicate this work to each one of them.

I also would like to thank the Federal University of Uberlândia (UFU) and the Faculty of Mechanical Engineering (FEMEC) for providing a high-level academic formation that made possible the elaboration of this manuscript.

I personally thank Prof. Dr. Odenir de Almeida, for all the advising and attention dedicated to this process and Reinaldo Tomé Paulino, for the amazing work in preparation of the physical model used in the experimental analysis.

Furthermore, I express my gratefulness to Roberta Cabral Maciel, for all the love and support that guided me through both easy and difficult times. This work is also dedicated to her father, Paulo Roberto Maciel Maia, who left us to fly beyond unexplored horizons.

CICELINI, G. **Numerical and Experimental Analysis of the Flow Over an eVTOL Concept.** 2022. 84 p. Trabalho de Conclusão de Curso, Universidade Federal de Uberlândia, Uberlândia.

RESUMO

Os veículos denominados eVTOLs (veículos elétricos de decolagem e pouso vertical) prometem ser o futuro do transporte urbano de pessoas e mercadorias. Empresas de diversos países atualmente estudam e desenvolvem seus próprios modelos, sempre priorizando eficiência energética e aerodinâmica. Este trabalho apresenta uma análise de alguns dos conceitos mais promissores em desenvolvimento, bem como a proposta de um novo layout baseado nas características mais vantajosas dos modelos já existentes, seguido de um estudo numérico e experimental do escoamento ao redor deste novo conceito. Simulações são implementadas utilizando as equações de Navier-Stokes médias (RANS) no software Ansys com o modelo de turbulência k-ε realizable de duas equações; a malha é constituída de elementos tetraédricos. O layout proposto foi construído em software CAD e impresso em escala, em impressora 3D. O modelo em escala de 1:27 foi colocado no túnel de vento, retornando dados referentes à sustentação, arrasto e pressão aerodinâmica, que posteriormente são comparados com os resultados numéricos. A solução computacional é preparada para o modelo reduzido, em velocidades relativas do ar mais baixas, em torno de 20 metros por segundo, coerentes com o voo de um eVTOL. A similaridade dos resultados numéricos com os experimentais é discutida, obtendo-se um bom nível de coerência entre as duas abordagens de ensaio. Este trabalho visa servir como referência para análises futuras na área de veículos do tipo eVTOL. Desse modo, um estudo mais detalhado de *setup* numérico (malha e *solver*) e a aplicação de outras rotinas experimentais é recomendado. A investigação dos efeitos de modificações na geometria, bom como a proposta de novos designs e conceitos, são sugeridas para as próximas etapas.

Palavras-chave: eVTOL; Aeronave elétrica; Aerodinâmica externa; CFD; CAD; Túnel de vento.

CICELINI, G. **Numerical and Experimental Analysis of the Flow Over an eVTOL Concept.** 2022. 84 p. Undergraduate Conclusion Thesis, Federal University of Uberlândia, Uberlândia.

ABSTRACT

Vehicles called eVTOLs (electric vertical take-off and landing vehicles) promise to be the future of urban transport of people and products. Companies from different countries study and develop their own models, always prioritizing energy efficiency and aerodynamics. This work presents an analysis of some of the most promising concepts under development, as well as the proposal of a new layout based on the most advantageous characteristics of the existing models, followed by a numerical and experimental study of the flow around this new concept. Simulations are implemented using Navier-Stokes equations (RANS) in the Ansys software with the two-equation realizable k-ε turbulence model; the mesh is constructed of tetrahedral elements. The proposed layout was built in CAD software and scale printed in a 3D printer. The 1:27 scale model was placed in the wind tunnel, returning data regarding lift, drag and air pressure, which are later compared with the numerical results. The computational solution is prepared for the reduced model, at lower relative air speeds, around 20 meters per second, consistent with the flight of an eVTOL. The similarity of the numerical results with the experimental ones is discussed, obtaining a good level of coherence between the two test approaches. This work aims to serve as a reference for future analysis in the area of eVTOLs. Thus, a more detailed study of numerical setup (mesh and solver) and the application of other experimental routines is recommended. The investigation of the effects of changes in geometry, as well as the proposal of new designs and concepts, are suggested for the next steps.

Key-words: eVTOL; Electric aircraft; External aerodynamics; CFD; CAD; Wind tunnel.

LIST OF FIGURES

LIST OF TABLES

SUMMARY

CHAPTER I

Introduction

According to the Encyclopedia Britannica (2013), the word “VTOL” is the abbreviation for vertical take-off and landing, and it describes any aircraft capable of taking off and landing in areas that only slightly exceed the overall dimensions of the aircraft [10].

Several projects of VTOL aircrafts were developed and tested throughout the history of aviation. Conceived by Stanley Hiller, the Hiller X-18 was one of the first documented VTOL experimental aircrafts. The wings where the engines were mounted could rotate and operate in the vertical plane, allowing the aircraft to take off and land like a helicopter, but also to fly horizontally like a conventional airplane.

Figure 1.1: The Hiller X-18

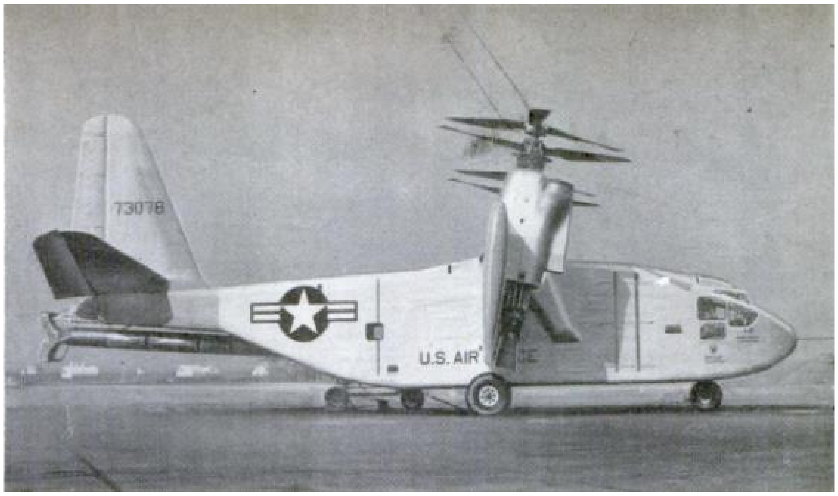

Source: Popular Mechanics Magazine, March 1959

Some decades after the first tests with the X-18, the British Royal Air Force implemented the Harrier in their operations. The Harrier is a jet aircraft which has the engines mounted horizontally, with their blast deflected downward to provide vertical thrust for vertical take-off and landings or backward to provide thrust for conventional flight. The Harrier achieves high subsonic speeds when in level flight.

Figure 1.2: British Royal Air Force Harrier GR7a at the Royal International Air Tattoo, Fairford, Gloucestershire, England.

Source: Encyclopedia Britannica, 2021.

The concept of an aircraft that could take off and land without needing a relatively long land strip arouse the attention of those concerned about the urban mobility. The urban transport modal of great megalopolises around the world could definitely take advantage of VTOL aircrafts.

Since one of the main concerns of the humankind nowadays is the reduction in emissions of pollutants resulting from the burning of fossil fuels, the concept of Electric Vertical Take-Off and Landing aircrafts (eVTOLs), took place as the main goal of several companies and joint ventures. The main idea behind many of these projects is to make air-taxi operations a reality, so they can work in conjunction with current urban transport systems, always prioritizing safety, sustainability and efficiency.

The development of eVTOL aircrafts is a completely new path to be trodden, and it will present new challenges in addition to those requirements already known by the big companies in the aviation branch. These challenges have been noted by those who search to develop new concept eVTOL aircrafts, like the autonomy of the power supply (batteries), the possibility of autonomous piloting, acoustic footprint, safety issues and how to diminish them, and many others.

Among the designs currently presented by the leading companies in that segment, some are more attractive than others. Those who present low rotor configuration, for example, convey the feeling that accidents could occur when a passenger tries to get to the cabin. Also, the concepts endowed with conventional wings in addition to the rotors tend to transmit a feeling of trust for offering a glide ratio in case of engine failure, while the projects that present drone configuration do not provide this additional safety feature.

According to Stoll et al. (2014), the Distributed Electric Propulsion (DEP) system is another feature that contributes to the overall efficiency of the vehicle, especially when dealing with small aircrafts, like the one proposed by this thesis.

Figure 1.3: eVTOL concept “Joby S2” (defunct), which presented DEP system.

Source: https://www.core77.com/posts/36900/How-Distributed-Electric-Propulsion-Will-Change-the-Way-We-Design-Flying-Vehicles, 2021

The motivation for this work is to analyze different kinds of eVTOL designs presented by different companies nowadays, aiming to develop a new concept that brings around the best features observed in the most promising designs. Characteristics as the construction materials, dimensions, passenger capacity, range, cruise speed and many others, will guide the parsing.

After the determination of a baseline and all necessary parameters of this new aircraft, a model will be conceived in CAD environment. This prototype will be printed in scale through additive manufacturing and experimented in the wind tunnel, so it is possible to verify the aerodynamic coefficients of the model, as well as the pressure throughout some points of the fuselage.

In parallel, a numerical analysis will be conducted in CFD software, were the same scale printed model will be submitted to similar flow and the results will be compared at the end.

A new eVTOL concept, as said, will be confronted with many challenges, and this work will focus on the aerodynamic analysis of a prototype. The interaction between wing and the propulsion system, the flow behavior over the vehicle’s body as well as the basic aerodynamic parameters evaluation intend to make possible the development of a promising design capable of face the real-world requirements.

CHAPTER II

Bibliographic Review

2.1. Previous Works

The study of eVTOL concepts and the flow-structure interactions had been mostly conducted in an industrial environment. Therefore, there is a relatively small number of articles regarding this topic. However, as the eVTOL study advances towards a tangible reality, is expected that more analysis will be taking place among the academics and hopefully, it will lead to the emerging of new technologies.

With all the variety of designs proposed for eVTOL concepts, the question about which would be the best configuration appears. Bacchini and Cestino (2019) discussed the advantages and disadvantages of all different categories, from the first concepts developed in the fifties and sixties to the present eVTOL configurations. In a more practical analysis, they selected three aircrafts (E-Hang 184, Wisk Cora and Lilium) and estimated several dimensions of each concept through pictures. The data was used to build up information like the total energy required for a considered mission and the drag polar of each aircraft. This study revealed that the best eVTOL configuration depends on the mission, once short-ranged missions are best fitted by multirotor designs due to the better hover performance, while long-range missions require more range capability.

Within the industry environment, some studies aim to optimize concepts in development. Lopez et al. (2019) conducted the optimization of a Rolls-Royce eVTOL concept wing. The surface was parametrically modeled and meshed in a computational environment, then an optimization turned to drag reduction was implemented through Rolls-Royce code package (HYDRA and SOFT Optimization Library). Having achieved a high-performing cruise shape for the wing, the authors expect to extend this technique to the fuselage geometry study.

Another discussion among the vastity of subjects concerning eVTOL concepts is the rotor-rotor interaction, a significant behavior when dealing with distributed propulsion. In a more recent work, Piccinini et al. (2020) described a numerical activity that aimed to the systematic study of the rotor-rotor aerodynamic interaction analyzed in typical eVTOL flight conditions. A novel mid-fidelity aerodynamic solver based on vortex particle method was implemented to show a noticeable reduction of the propeller's performance in side-by-side configuration, while a tandem configuration was responsible for a loss of thrust in the order of 40% and a propulsive efficiency reduction of about 20%.

The aerodynamic modeling of an eVTOL concept is also a complex process. Simmons and Murphy (2021) recently conducted the implementation of a methodology to develop a high-fidelity aerodynamic model for the Langley Aerodrome No. 8 (LA-8), a tandem tilt-wing, distributed electric propulsion eVTOL concept. Two novel system identification-based approaches were used to develop an aerodynamic model for the LA-8 vehicle using wind tunnel data. The modeling strategies were compared by assessing their predictive performance for validation data acquired separately from the data used to identify the model, and a sufficient predictive capability was proven.

Some works conducted in Brazil are also present in this bibliographic review. Varges (2018) proposed a conceptual study of an eVTOL for massive urban transport. This thesis covered the initial review of eVTOL concepts, preliminary calculations to define topics like aircraft layout, powerplant and flight mechanics. At the end, a model was proposed and the major challenges for its implementation were discussed.

The second Brazilian dissertation involving eVTOL-related concepts is a research over distributed propulsion and the aerodynamic effects due to propulsion/wing interaction, written by Silva Filho (2020). Aiming to analyze those interactions, numerical methods based in Reynolds-Averaged Navier-Stokes equations were implemented, including the k-ω SST turbulence model and an actuator disk model based on blade element theory which represented propulsion. The results were validated with experimental data found in specific literature and proved to show good representation of the physics involved in the studied flow, especially in wing regions which were directly affected by the propulsion flow-field.

Another proposal of study concerning the concept of eVTOLs was developed by Balli (2020), which presented a method for preliminary sizing of an eVTOL, considering the aircraft as the sum of several building blocks and estimations for the weight of each component. A preliminary review of existent models was the base for configuration comprehension, as well as mission profiles. A methodology to estimate weight, drag and power was described and compared to wind tunnel tests, which has proven to be general and allowing the analysis of a wide variety of configurations.

Regarding the acoustic footprint of an eVTOL, Higgins, Barakos, Shahpar and Tristanto (2020) investigated the acoustic behavior of an aircraft using a CFD solver. After modeling the vehicle and meshing the model with the chimera grid method, the group could provide a significant knowledge of the noise profile around the fuselage cabin. That led to an optimization study that aimed to reduce the amount of noise generated by the eVTOL concept in study.

2.2. Ongoing Projects

In this section, some of the most promising projects in eVTOL category are gathered for posterior comparison. One of them technically is not an eVTOL but a hybrid VTOL. In spite of that, it is also included here for its remarkable characteristics.

These projects are what the companies presented of more advanced until the moment that this thesis is being written. Other concepts are expected to emerge in the next years, for the idea of electric flying vehicles being able to execute air taxi missions is already consolidated as the future of urban transportation.

2.2.1. Airbus CityAirbus

The CityAirbus is a four-passenger, autonomously piloted eVTOL vehicle designed by Airbus for urban air mobility. Eight rotors are powered by eight Siemens SP200D direct-drive 100 kW units relying on four 140 kW batteries developed by Airbus Defense and Space arm.

The aircraft will carry up to four passengers with a cruise speed of 120 km/h (75 mph), currently having 15 minutes of flight time. Each powertrain is composed of a carbon fiber ducted co-axial fixed-pitch propellers of 2.8 meters (9.2 ft) of diameter, providing 400 kg (881 lb.) of thrust for a payload of up to 250 kg (551 lb.).

Figure 2.1: The CityAirbus concept.

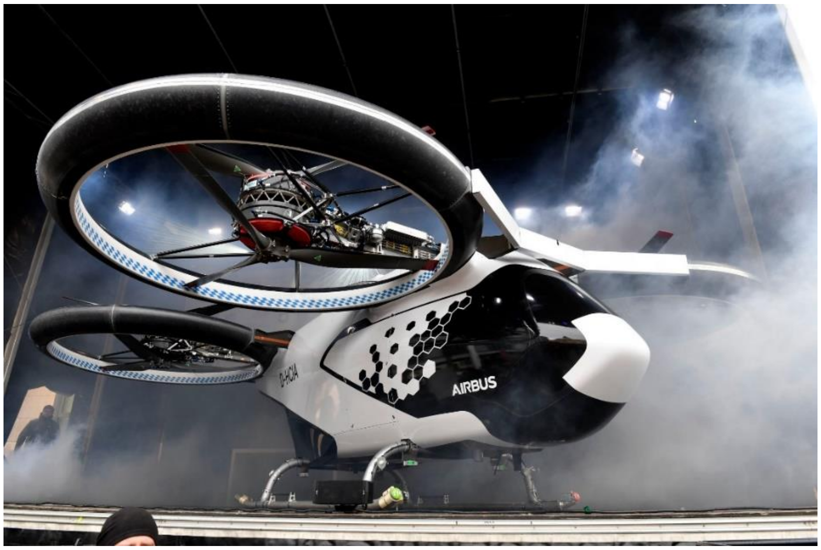

Source: https://evtol.news/airbus-helicopters/

The CityAirbus is intended for flying between fixed routes between critical transit hubs, like downtown to an airport or seaport. It has already accomplished test flights with an unmanned full-scale remote-controlled demonstrator. Its dimensions are 8 m x 8 m (26.2 ft x 26.2 ft) length and width, and it has a take-off weight of 2.2 tons.

2.2.2. Archer (unnamed project)

Archer Aviation company has been developing multiple models of eVTOL aircraft focused on improving mobility in cities. Their five-seat eVTOL aircraft (which has not been named yet) will carry four passengers and one pilot, and a sub-scale two-seater demonstrator called Maker is being developed by Archer.

The aircraft has a DEP system of twelve electric rotors: six tilt-propellers (each with five blades) for forward and VTOL flight, and six fixed propellers for VTOL-only flight (each propeller having two blades). The sleek fuselage is endowed with high main wing, a V-tail and tricycle fixed wheeled landing gear.

Figure 2.2: The Archer Maker eVTOL concept.

Source: https://www.archer.com/news#contact-form

This vehicle has a projected cruise speed of 241 km/h (150 mph), maximum range of 96.5 km (60 miles), cruise altitude of 610 meters (2,000 ft) and MTOW of 3,175 kg (7,000 lb). According to the company, the aircraft will produce a 45-dB noise during forward flight. Data available from the Archer website shows an aerodynamic efficiency (L/D) of 11.3.

Figure 2.3: Front view of the Archer Maker concept.

Source: https://evtol.news/archer

Figure 2.4: A top close view of the Archer Maker wings.

Source: https://www.archer.com/news#contact-form

2.2.3. EHang 216

The EHang 216 is an improved eVTOL design by the Chinese company EHang, derived from the EHang 184. It presents eight arms (instead of four, like the 184 version), each arm holding two electric motors with counter-rotative propellers. Hence, it has DEP system with sixteen powertrains total. The landing gear is a fixed skid type.

The whole concept is very similar to a conventional drone, at least visually. That implies that passengers must be careful when entering the aircraft, once the rotors are located directly in the path of the embarking and disembarking.

The EHang 216 has two seats and it is an autonomous aircraft, so it can carry up to two passengers, without the need of an experienced pilot. According to the company, this aircraft accomplished several flight tests, some of them in low visibility conditions.

The company also provides some reference specifications, such as: 1.77 m (5.8 ft) of height, 6.61 m (21.7 ft) of width, cruise speed of 100 km/h (62 mph), maximum speed of 130 km/h (80.8 mph), maximum altitude of 3,000 m (9,843 ft), maximum payload of 220 kg (485 lb.) and range with maximum payload of 35 km (22 miles).

Figure 2.5: The EHang 216.

Source: https://www.helicopterspecs.com/2019/10/ehang-216.html

2.2.4. EHang VT-30

The EHang VT-30 is another eVTOL project by the Chinese company EHang. Unlike the other EHang eVTOL, 216, the VT-30 is an aircraft with a more conventional design. That means it has one main low wing, horizontal and vertical stabilizers mounted in an inverted V-tail boom and an electric pusher-propeller for forward flight.

Figure 2.6: The EHang VT-30.

Source: https://evtol.news/ehang-vt30

The VTOL operation is possible due to four groups of two counter-rotative propellers each, totalizing eight VTOL propellers. Each propeller, including the pusher, has its own electric motor.

The aircraft is capable of carrying two passengers, once the piloting is totally autonomous. The range is informed to be about 300 km (186 miles), the maximum flight time is 100 minutes and its empty weight is 700 kg (1,543 lb.). The fuselage is made of carbon fiber composite and the landing gear is a fixed tricycle wheeled type.

Figure 2.7: Lateral and top of the VT-30.

Source: Composition made with images from https://evtol.news/ehang-vt30

2.2.5. EmbraerX Eve

The Eve is an eVTOL concept in development by EmbraerX, the disruptive innovation subsidiary of the Embraer Group. Despite being in its early phases of development, Eve already got a subscale demonstrator vehicle, remote controlled, which already accomplished some test flights.

Figure 2.8: An artistic conception of Eve.

Source: https://evtol.news/embraer/

The structure of the aircraft consists in the fuselage and two wings, being one main wing and one canard-like wing, and a landing gear system based on two helicopter-like skids. A vertical empennage with rudder is present, granting lateral stability.

Figure 2.9: Embraer EVE subscale demonstrator.

Source: https://insideevs.uol.com.br/news/496716/embraer-carro-eletrico-voador-brasil/

The vehicle is endowed with four electric-driven pair of rotors positioned in the horizontal plane, being responsible for the VTOL operations. An extra pair of electric-driven rotors located in the main wing, in a pusher configuration, are able to accelerate the aircraft so it achieves cruise speed. Hence, its DEP system totals ten powertrain groups, although the final project may suffer some modifications, like getting only one forward flight powertrain.

Some parameters of this project are yet to be defined, but the company is aware of some preliminary characteristics. The Eve will be capable of carrying four passengers plus baggage, in addition to its probable weight of 1 ton. The partnership between EmbraerX and Uber requires a cruise speed of 241 km/h (150 mph) and a range of at least 96 kilometers (60 miles). The cruise altitude is meant to stay between 800 to 1,000 meters (2,600 to 3,300 ft.).

2.2.6. Horizon Aircraft Cavorite X5

The Cavorite X5 is a hybrid VTOL concept in development by the Canadian company Horizon Aircraft. The most distinct feature in this concept is the location of the VTOL fans. Unlike the other eVTOL projects in this group, the Cavorite X5 has a hybrid-electric gas engine to create electricity for all electrical systems on-board, a back-up motor in case the main gas engine fails and a battery pack system on-board.

Figure 2.10: The Cavorite X5 side view

Source: https://evtol.news/horizon-aircraft-cavorite-x5

The aircraft presents a rear high forward swept main wing and a forward swept rearward canard, both with winglets. Inside those wings are located sixteen ducted fans for VTOL flight (four in the canard and twelve in the main wing), which are covered with sliding surfaces while in forward flight. Then, one pusher propeller is responsible to make the aircraft achieve cruise condition.

This project is meant to carry one pilot and four passengers, has a cruise speed of 350 km/h (215 mph), a range of 500 kilometers (310 miles) with passengers and cargo and 1,000 kilometers (625 miles) without load. Regarding its dimensions, it has a length of 11.6 meters (38 ft.), a height of 2.8 meters (9.2 ft.) and a wingspan of 15.3 meters (50.3 ft.). The fuselage is made of carbon fiber composite, it presents a V-tail configuration and a wheeled retractable landing gear.

Figure 2.11: The Cavorite X5 with the wings open and then closed.

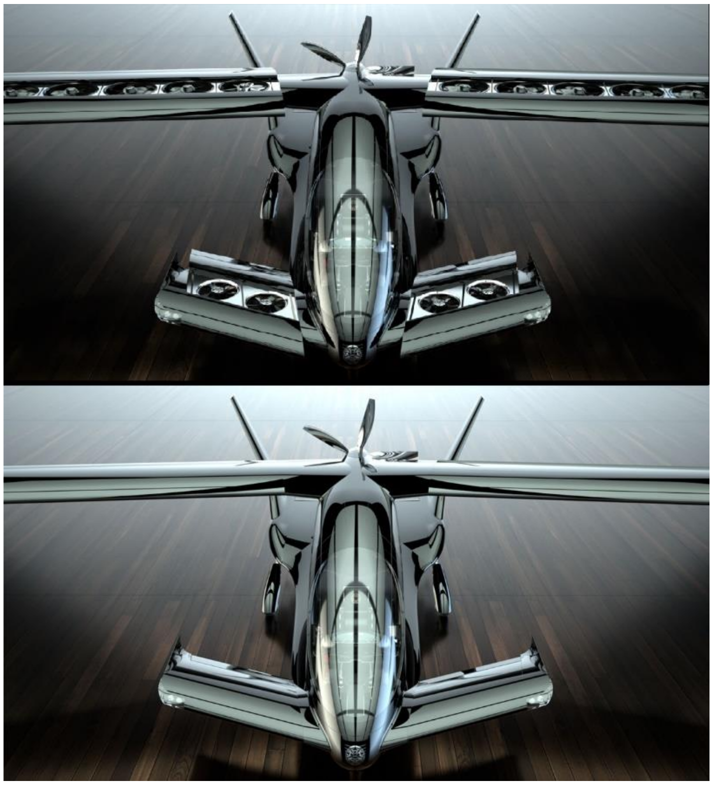

Source: Composition made with images from https://evtol.news/horizon-aircraft-cavorite-x5

2.2.7. Joby S4

The Joby S4 is the current eVTOL project by Joby Aviation, a venture-backed startup aerospace company located in Santa Cruz and San Carlos, California (USA). This current vehicle is the result of a continuous development, which passed through some former designs, such as Joby S2, Joby Lotus and Joby Monarch.

It is a five seat eVTOL which carries one pilot and four passengers, equipped with retractable tricycle landing gear and six tilting propellers located on both the fixed wing and its V-tail. Four of those propellers tilt vertically together with their motor nacelles, and the other two of them tilt using a linkage mechanism. This allows the aircraft to take off vertically and then assume a horizontal flight configuration, counting on the fixed wing to provide lift.

The DEP system is responsible to take this aircraft to speeds of 322 km/h (200 mph). The needed power comes from lithium-nickel-cobalt-manganese-oxide batteries, which provide a range of 241 kilometers (150 miles).

Figure 2.12: The Joby S4 in VTOL configuration.

Source: https://evtol.news/joby-s4

The Joby S4 also counts on a unified flight control system to reduce pilot workload during the conversion to and from VTOL to horizontal flight mode. The unified control system can take control of the aircraft in case of emergency during the flight, being able to land it safely without any intervention of the pilot.

Some flight tests were already conducted to verify the performance of the Joby S4. The current model presents a composite fuselage, wingspan of 10.7 meters (35 ft.), length of 7.3 meters (24 ft.) and weight of 1,815 kilograms (4,000 lb.). The electric supply system works with a reserve battery power to provide extra flight time in case of an unexpected delay during landing.

The following images present isometric views of the Joby S4. In Figure 2.13, the frontal view shows the symmetry lines that connect the spinner of the three pairs of rotors (when in cruise mode) and also the three planes where each pair is located, when in VTOL configuration.

Figure 2.13: Joby S4 frontal view in both VTOL and cruise configuration.

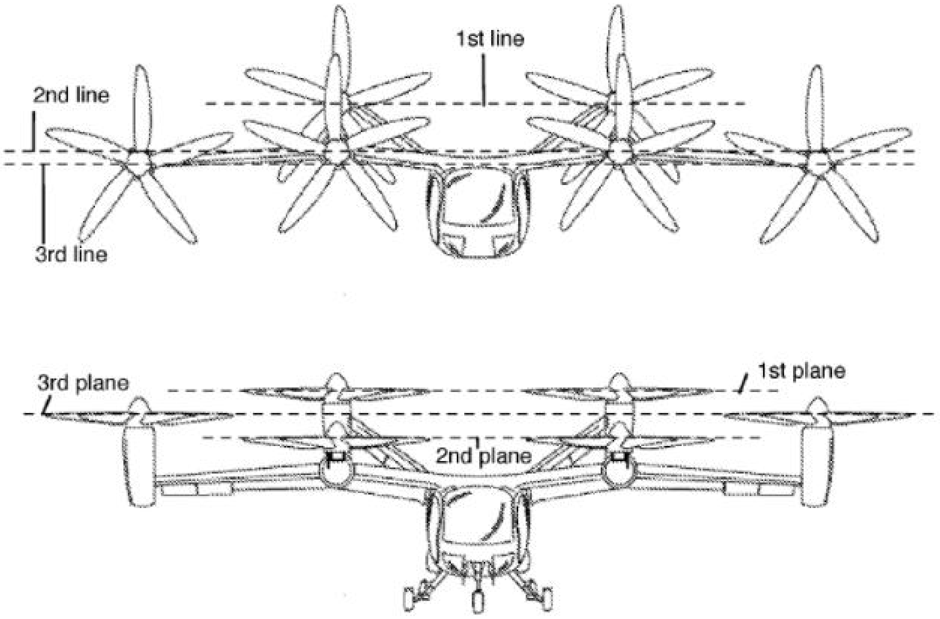

Source: https://evtol.news/news/inside-jobys-unicorn-flight-tests-and-patents-reveal-new-details

The next image illustrates the superior view of the aircraft, highlighting the distance between each symmetry line, in VTOL and cruise configurations as well.

Figure 2.14: Joby S4 superior view in both VTOL and cruise configuration.

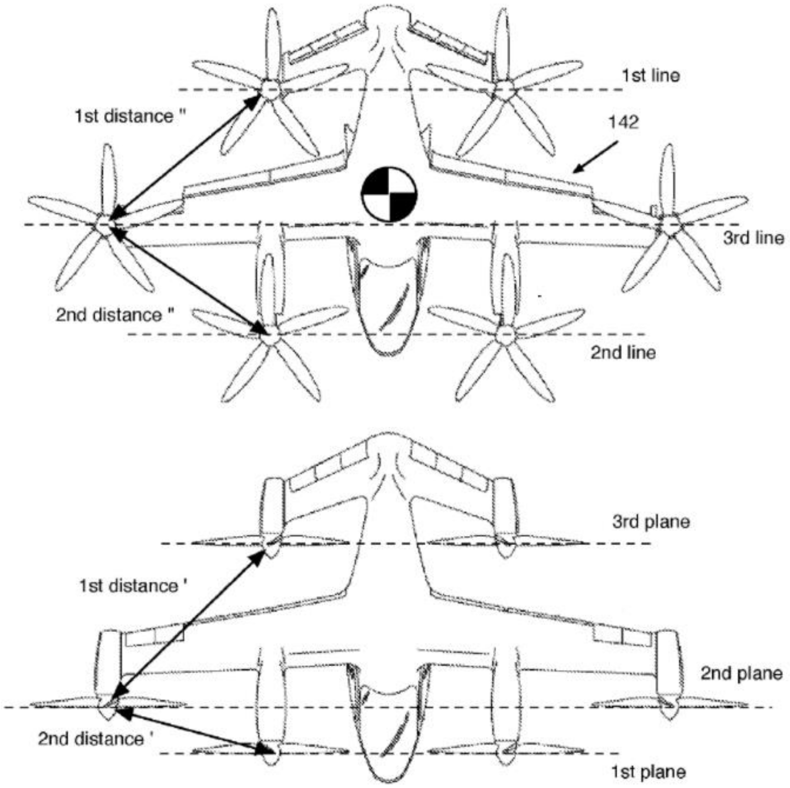

Source: https://evtol.news/news/inside-jobys-unicorn-flight-tests-and-patents-reveal-new-details

2.2.8. Lilium Jet

The Lilium Jet is one of the most promising eVTOL current projects in development, conducted by the German start-up Lilium GmbH. There are different configurations of this aircraft in study, but the main set consists of a five-seater canard eVTOL. It is based on distributed propulsion, where 36 electric ducted fans, each one having its own motor, are positioned along the main wing and the canard.

The electric ducted fans are located in pairs of three in the wings for a total of twelve fan units or flaps. There are two flaps on each forward wing and four flaps on each rear wing. Each flap can tilt independently of one another and operate at different speeds of each other, based on wind conditions during vertical flight, transitioning between vertical and forward flight, and during forward flight. Because of this, control surfaces as the rudder, for example, are not required, once the groups of flaps can easily maintain the stability of the aircraft in flight.

Figure 2.15: The Lilium Jet left-front size view in a hangar.

Source: https://evtol.news/lilium/

The position of the fans directly above the wing, in parallel to the fact that all the fans are mounted inside a duct, is responsible for the low noise rates verified during the tests of this eVTOL. Another perk of this layout is the ingestion of airflow, reducing the chance of detachment of the boundary layer during operation, favoring better aerodynamic characteristics and delaying the stall. This characteristic can be visualized in Figure 2.16, which shows the airflow over the wing in the three possible configurations: cruise flight, transition and VTOL operation.

Figure 2.16: Cut view of the Lilium Jet wing in three moments (cruise, transition and hover configuration).

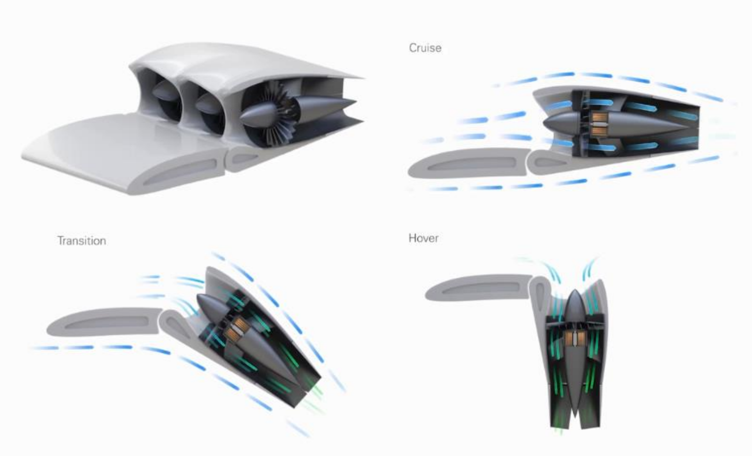

Source: https://lilium.com/jet

The Lilium Jet already accomplished more than one hundred flight tests, in which the aircraft was capable of traveling at speeds exceeding 100 km/h (62 mph), perform turns at bank angles of up to 30 degrees and climb and descend vertically at rates of 152 meters (500 ft) per minute. It is also at the certification process, being certified as a fixed wing aircraft with EASA and FAA.

The 5-seater Lilium Jet is meant to present a cruise speed of 280 km/h (175 mph), maximum range of 250 kilometers (155 miles) plus reserves and a maximum flight time of 60 minutes. It has a tricycle fixed landing gear, a wingspan of 13.9 meters (45.6 ft.) and a length of 8.5 meters (27.9 ft.)

Figure 2.17: The 3 views of Lilium Jet 7-seater version.

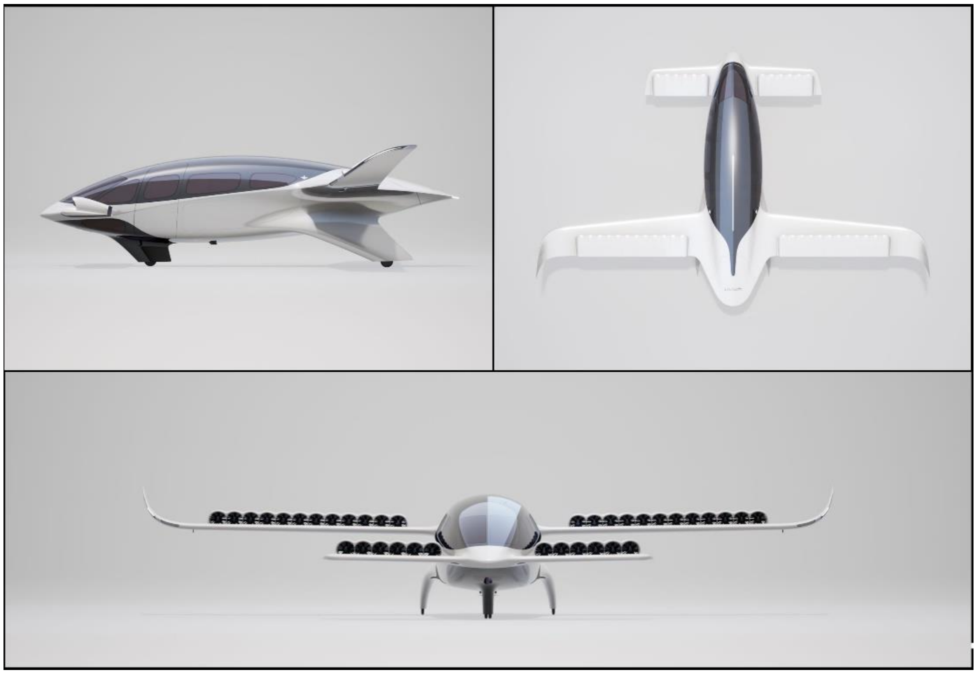

Source: Composition made with images from https://lilium.com/newsroom-detail/technology-behind-the-lilium-jet

2.2.9. Terrafugia TF-2A

The TF-2A is the current eVTOL design in study by Terrafugia. A sub-scale model test flight occurred in mid-December 2019 to validate this concept, presenting a wingspan of 4.5

meters (14.8 ft.), maximum take-off weight of 60 kilograms (132 lb.), and a cruising speed of about 100 km/h (62 mph).

Figure 2.18: The Terrafugia TF-2A concept.

Source: https://evtol.news/terrafugia-tf-2a/

The aircraft presents a DEP system with eight lift-propellers and one rear pusher-prop for forward flight. A main high wing with ailerons and a twin boom tail are also evident. The TF-2A has a wingspan of 4.5 meters (14.8 ft.), composite fuselage and a fixed tricycle landing gear.

The full-scale version is meant to have a cruise speed of up to 180 km/h (112 mph), a maximum range of 100 kilometers (62 miles), capacity for one pilot, two passengers and luggage and a maximum payload weight of 200 kilograms (441 lb.). The MTOW is 1,200 kilograms (2,646 lb.) and the cruise altitude is 3,000 meters (9,843 ft).

Figure 2.19: Size comparison of the TF-2A with a 1.85-meter-tall adult.

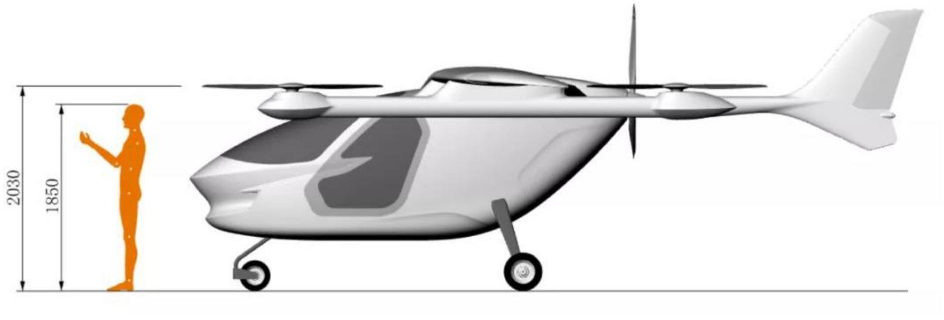

Source: https://evtol.news/terrafugia-tf-2a/

Figure 2.19 shows that the vertical propellers are higher than the usual passengers, at a height of 2.03 meters (6.7 ft.), keeping ground crew and passengers safe from embarking and disembarking accidents.

Figure 2.20: Front view of the TF-2A.

Source: https://evtol.news/terrafugia-tf-2a/

2.2.10. Vertical Aerospace VA-X4

The VA-X4 is one of some eVTOL concepts in development by the English company Vertical Aerospace. This project is very similar to the Archer concept, presenting a V-tail with rudders and a high gull wing with flaps and ailerons where the DEP system is located. About its wing, the tips are both considered winglets and anhedral surfaces.

Figure 2.21: The VA-X4 concept.

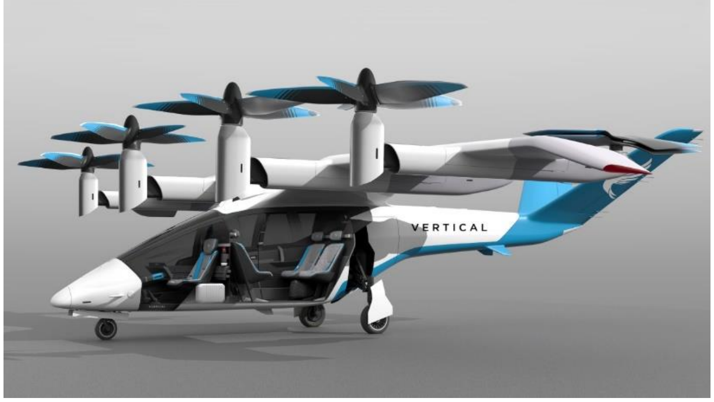

Source: https://evtol.news/vertical-aerospace-VA-1X

Like the Archer concept, this aircraft has a group of four electric-driven tilt-propellers for VTOL and forward cruise flight and a group of four rear-wing horizontal-placed rotors exclusive dedicated to VTOL operation. The powertrain was co-developed with Rolls-Royce.

According to the Vertical Aerospace company, the VA-X4 achieve noise levels of 45 dB at cruise flight and 60 dB while in hover mode. It will carry one pilot and four passengers, has a cruise speed of 241 km/h (150 mph), a top speed of 325 km/h (202 mph), a maximum range of over 161 kilometers (100 miles) and maximum payload of 450 kilograms (992 lb.). Its wingspan is 15 meters (49.2 ft.), the length is 13 meters (42.7 ft.) and the height is 4 meters (13.1 ft.).

The VA-X4 presents a retractable tricycle landing gear. Its airframe is made of carbon composite material and allows three possible configurations: passenger, cargo and medical transport.

Figure 2.22: 3-view image of the VA-X4 concept.

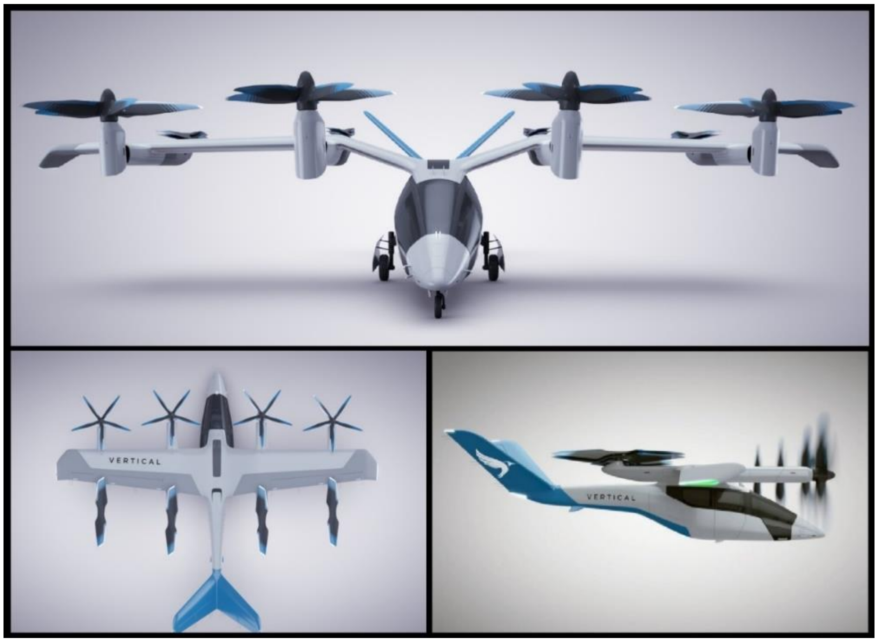

Source: Composition made with images from https://evtol.news/vertical-aerospace-VA-1X; https://saudigazette.com.sa/article/597142; https://www.flightglobal.com/aerospace/why-vertical-aerospace-thinks-f1-know-how-will-put-it-in-pole-position/143018.article.

2.2.11. Volocopter VoloCity

The VoloCity is an eVTOL project in its fourth-generation design, conducted by the German company Volocopter GmbH. The aircraft has a DEP system of eighteen small fixed-pitched propellers and eighteen electric motors on top a beam structure, which keeps a free path for embarking and disembarking. Flight control is made by varying the speed of each eighteen propellers independently.

Figure 2.23: The VoloCity concept.

Source: https://evtol.news/volocopter-volocity/

According to the company, the aircraft produces 65 dB when hovering at 75 meters (246 ft.) above the ground. VoloCity has room for one pilot and one passenger plus luggage, has a maximum speed of 110 km/h (68mph) and a cruise speed of approximately 90 km/h (56 mph). Its range is 35 kilometers (22 miles) and the MTOM is 900 kilograms (1,984 lb.), of which the maximum payload is 200 kilograms (441 lb.).

Regarding the structure of the VoloCity, it presents a carbon composite fiber structure, fixed skid landing gears and an overall height of 2.5 meters (8.2 ft.). The diameter of the rotor rim including rotors is 11.3 meters (37 ft.) and excluding them will give a diameter of 9.3 meters (30.5 ft.). Hence, the diameter of each rotor is 2.3 meters (7.5 ft.).

Figure 2.24: Different viewing angles of the VoloCity concept.

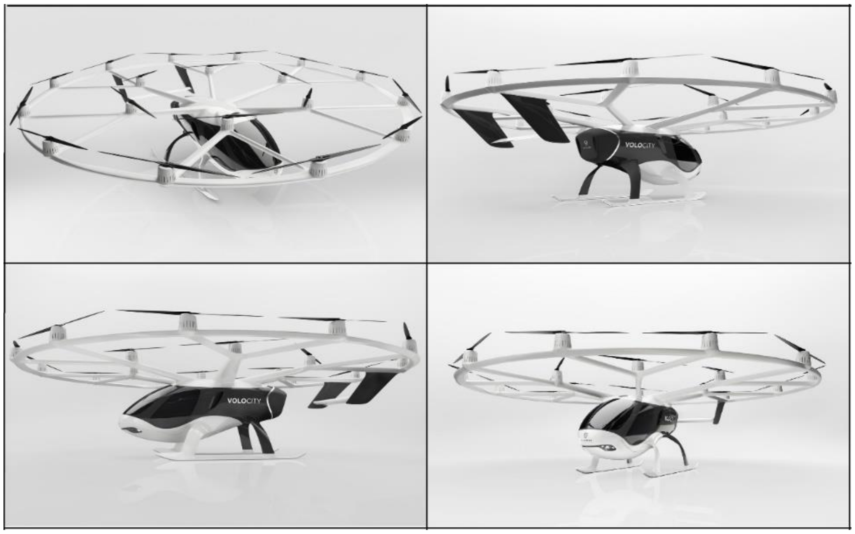

Source: Composition made with images from https://evtol.news/volocopter-volocity/

2.2.12. Wisk Cora

Cora is the first eVTOL aircraft developed by the joint venture Wisk, formed by The Boeing Company and Kitty Hawk Corporation. Cora is a two-passenger autonomous vehicle with twelve independent electric-powered lifting propellers mounted on its 11 meters (36 ft.) long wings, for VTOL operations. Another three-bladed pusher propeller provides thrust for forward flight.

Figure 2.25: A side view of the Cora.

Source: https://www.helicopterspecs.com/2019/10/ehang-216.html

As said, this aircraft is completely autonomous and can carry up to two passengers, has a cruise speed of 160 km/h (100 mph), a range of 40 kilometers (25 miles) plus reserves and a total flight time of 19 minutes with a 10-minute reserve. The cruise operation altitude is between 457.2 to 1524 meters (1,500 to 5,000 ft.) above the ground, although it can achieve a maximum altitude of 3.04 kilometers (10,000 ft). Its maximum payload is 181 kilograms (400 lb.)

The Cora is 6.4 meters (21 ft.) long and has a wingspan of 11 meters (36 ft.). It presents a twin book tail with inverted U horizontal stabilizer, a wheeled tricycle fixed landing gear and a parachute system in case of catastrophic failure.

Figure 2.26: Isometric and 3-view representation of the Cora.

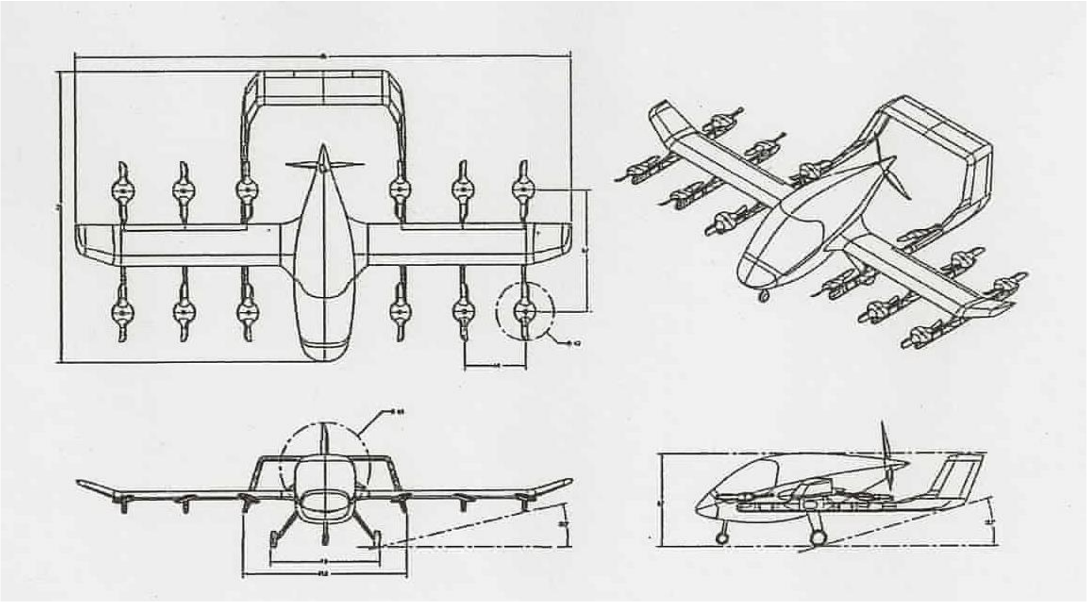

Source: https://evtol.news/kitty-hawk-cora/

CHAPTER III

Methodology

This chapter is designated for the presentation and definition of the proposed eVTOL model, and the numerical and experimental setups used on this study.

3.1. Previous concepts analysis

Before the definition of which characteristics will be applied in the concept of this study, it is convenient to analyze the main technical features observable in all the eVTOLs mentioned earlier. The following table diagrammatize the most important characteristics in each model.

Table 3.1: Main features of the studied eVTOLs.

Vehicle	Layout Configuration	Wing Position	Propulsion System	Number of Occupants	Tilting Components	Landing Gear
Airbus CityAirbus	Drone	-	DEP	4	No	Fixed skid
Archer (Unnamed)	Wing	High	DEP	5	Yes	Fixed tricycle
EHang 216	Drone	-	DEP	2	No	Fixed skid
EHang VT-30	Wing	Low	DEP	2	No	Fixed tricycle
EmbraerX Eve	Wing (canard)	High	DEP	4	No	Fixed skid
Horizon Aircraft Cavourite X5	Wing (canard)	Low	Distributed (Hybrid)	5	No	Retractable tricycle

Joby S4	Wing	High	DEP	5	Yes	Retractable tricycle
Lillium Jet	Wing (canard)	Mid	DEP	5	Yes	Fixed tricycle
Terrafugia TF-2A	Wing	High	DEP	3	No	Fixed tricycle
Vertical Aerospace VA-X4	Wing	High	DEP	5	Yes	Retractable tricycle
Volocopter VoloCity	Drone	-	DEP	2	No	Fixed skid
Wisk Cora	Wing	Low	DEP	2	No	Fixed tricycle

Source: Own authorship.

Most of the concepts presented in the table have a wing configuration, combined with the DEP system. This layout delivers a more efficient horizontal flight, since it takes advantage of the aerodynamic properties of the wing. It also eliminates the necessity of moving parts, since the vehicle usually have rotors for the VTOL operation and an additional propeller for horizontal flight.

All the different layouts show that those with high wing configuration, with the rotors out of range for the occupants, propose a safer design. Reducing the risk of accidents involving people hitting in-movement rotors is one of the objectives of the new concept to be presented.

Regarding the landing gear system, there are advantages and disadvantages of each type. A retractable landing gear reduces drag while in flight but adds moving parts that can present malfunctioning and makes the maintenance more laborious. A fixed landing gear, although it provides more drag, makes up for being easier to maintain and operate, beyond reducing the project’s financial cost.

With all those considerations, the baseline geometry chosen for this study was a mix of Wisk Cora and Terrafugia TF-2A designs. Both concepts gather most of the desirable characteristics in an eVTOL project and the 3-view blueprint of the Wisk Cora was found in online database, making it easier to build a detailed printable model in the CAD environment.

3.2. Conceptual design

Following the steps of initial phases in aircraft design described by Raymer (2018) and keeping in mind considerations made upon the review of previous eVTOL concepts, it is necessary to start defining the vehicle requirements and initial estimates for layout, weight, payload capacity, among others.

3.2.1. Aircraft mission

The mission of this aircraft is to be an air taxi. Once that the vehicle will be 100% electric and the baseline for this project will be the Wisk Cora, an estimated range of 40 kilometers (25 miles) is close enough to the concept's reference.

In order to validate the viability of this range, it is possible to compute the distance between two points of interest in a metropolis of choice. In Figure 3.1 it is possible to estimate the linear distance between São Paulo downtown and Barueri, which is approximately 25,1 kilometers (15,6 miles). Therefore, this one of the interest routes that could be operated by the aircraft in study.

Figure 3.1: Distance line between Barueri and São Paulo downtown.

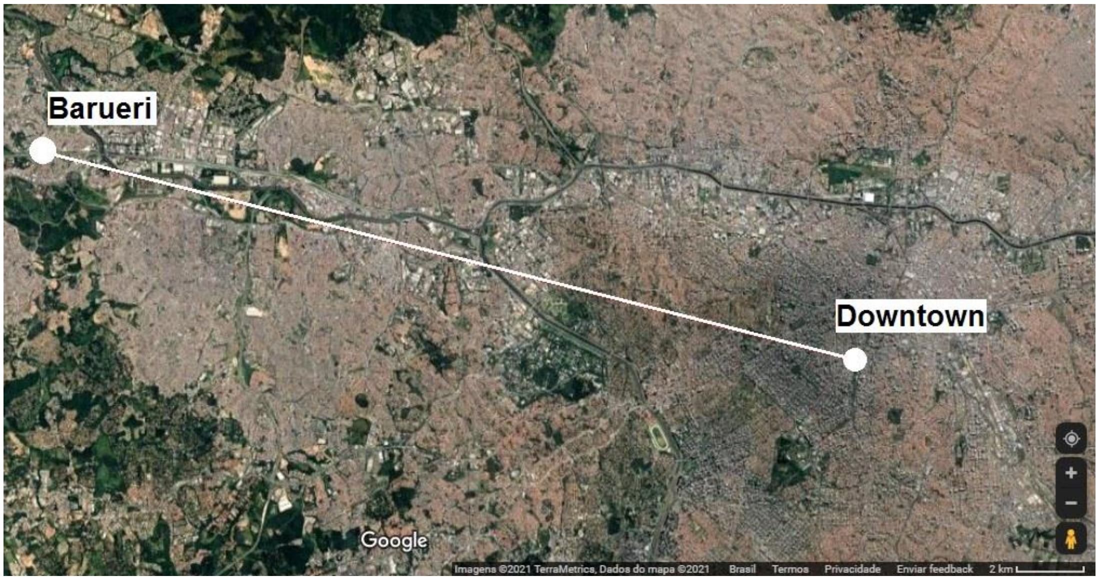

Source: Composition made with images from Google, 2021.

Like the reference aircraft, an estimated maximum payload of 180 kilograms (397 lb.) is also a goal to achieve.

3.2.2. Wing and stabilizers

The aircraft will have the hybrid layout, combining a conventional wing with VTOL rotors, while a rear propeller will be responsible for horizontal flight. The empennage will follow the twin book design with inverted U horizontal stabilizer. The pre-selected airfoil for the wing and for the horizontal empennage is the NACA 2412 (Figure 3.2). Since this is a conceptual approach, possible unsatisfactory results produced by all the choices made at this point may require future modifications.

Figure 3.2: The chosen aerodynamic profile (NACA 2412).

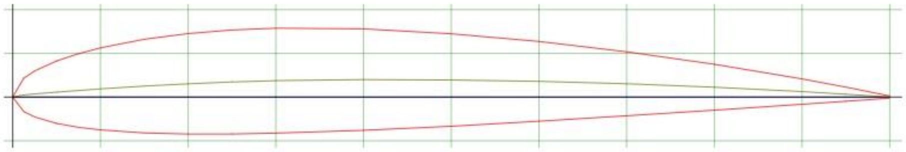

Source: Airfoil Tools website (2021).

An important concern about safety contributed for the high wing configuration, which was selected so the rotor plane no longer intersects occupants walking by the aircraft. These occupants are supposed to have an average human being height, 1.85 meters (approximately 6 feet), so the base of all the rotors must stay at least 2 meters (6.56 feet) from the ground when the eVTOL is landed.

For the first estimate to the aspect ratio, a projected wingspan of 10 meters (32.8 feet) and a wing area of 9 m^2 (96.8 ft^2) will be considered. These values were estimated through the upper view of the Wisk Cora. That way, we have the aspect ratio given by:

$$A = \frac{b}{s} \tag{3.1}$$

$$A = \frac{10^2}{9} = 11.1$$

According to the literature, the greater the aspect ratio, the greater the rate of variation of the lift coefficient in relation to the variation angle of attack, which helps in terms of comfort (flight with lower angle of attack) and propulsion efficiency (smaller angle of attack implies greater horizontal thrust component and less overall drag). This is shown in the figure below, which evidences aspect ratio above 8 as the ideal.

Figure 3.3: Effect of aspect ratio on lift.

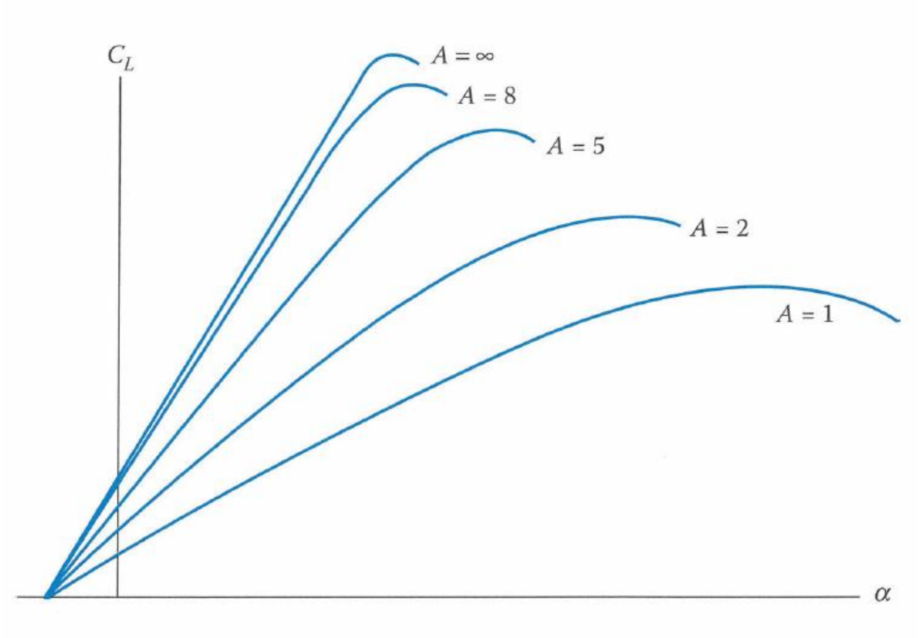

Source: Raymer (2018), page 77.

Since the speeds and altitudes to be reached by this aircraft are not so high due to the profile of the mission, the wing sweep value will be zero. Also, the wing taper ratio will be based on Cora’s design, which presents a lightly enhanced chord at the wing root that decreases to a constant value throughout the wing. That gives a taper ratio λ = 1.0.

Once the concept will be endowed with a high wing, a dihedral angle is not necessary according to the literature. This makes the construction process easier and less costly.

Figure 3.4: Dihedral guidelines.

	Wing Position		
	Low	Mid	High
Unswept (civil)	5 to 7	2 to 4	0 to 2
Subsonic swept wing	3 to 7	–2 to 2	–5 to –2
Supersonic swept wing	0 to 5	–5 to 0	–5 to 0

Source: Raymer (2018), page 89.

Following the baseline design, the wing incidence and the wingtip torsion will be close to zero. Since this is an experimental aircraft, the effects of choosing this configuration will be evaluated both in wind tunnel and in CFD software. The mentioned design also provides the wingtip form, which will be similar in this project.

Regarding the horizontal stabilizer, estimated dimensions for the span a chord are respectively 2.87 meters (9.41 feet) and 0.8 meters (2.62 feet). This gives a wing area of approximately 2.3 m^2 (24.8 ft^2) and the aspect ratio follows, accordingly to Equation 3.1:

$$A_{ht} = \frac{2.87^2}{2.3} = 3.58$$

Once the vertical stabilizer is doubled due to the tail design, the dimensions will be as closest as possible to the baseline.

3.2.3. Fuselage

The fuselage appearance must be similar to Cora's, so the vehicle will be designed for accommodating two passengers. This makes interesting for it to be autonomous and this feature must be discussed in the future.

3.2.4. Materials

The materials used in the construction of the final prototype will be composite materials that provide both strength and lightness. Some critical components, such as the longeron, must be composed of aluminum alloys commonly applied in the aeronautical environment.

3.2.5. Weight

According to the estimates regarding the total weight of the Wisk Cora proposed by Sigler (2020), a projected total weight for this new concept is going to be around 750 kilograms (1,653 lb.). This is approximately close to the weight of a Cessna 152, a general aviation small airplane.

3.3. CAD concept

Gathering all the defined features, dimensions and specifications stated until this point, a model was developed with the aid of CATIA v5.

The 3-view projection of Wisk Cora was used to guide the lines of this concept, which presents all the modifications intended to improve the original design. The final result is shown below. The detailed dimensions of the real scale model are available in Appendix I.

Figure 3.5: The eVTOL concept conceived in CAD environment.

Source: Own authorship.

Figure 3.6: Front view of the concept.

Source: Own authorship.

Figure 3.7: Side view of the concept.

Source: Own authorship.

Figure 3.8: Upper view of the concept.

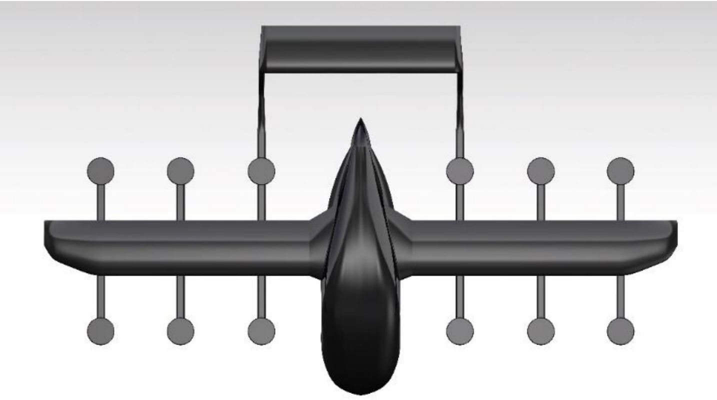

Source: Own authorship.

As it is possible to verify by the pictures, the vertical flight rotors were simplified as discs and the rear propeller blades were not included in this construction, intending to eliminate undesirable variables in the experimental and numerical analysis.

A comparison of sizes shows that, as intended, an average-sized person walking by or entering the aircraft will not have to worry about the rotors, for they will occupy a higher position when the eVTOL is on the ground. However, this will bring another issue, which is the necessity of a retractable step to help passengers to get on board.

Figure 3.9: Size comparison between the eVTOL and an average-sized human being.

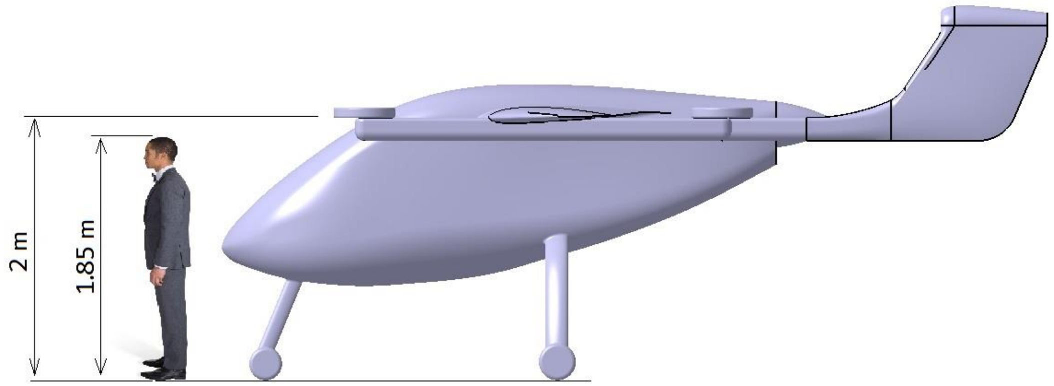

Source: Own authorship.

3.4. Experimental analysis

This section aims to present the conditions and setups on which were based all the experiments involving the wind tunnel and the physical 3D-printed model.

3.4.1. Wind tunnel calibration

The experimental analysis of the aircraft proposed in this work was meant to be conducted with the aid of a wind tunnel (TV-60), located in the Experimental Aerodynamics Laboratory (LAEx) of Faculty of Mechanical Engineering, Federal University of Uberlândia.

First of all, it was necessary to build the calibration curve of the tunnel. A pitot tube positioned inside the test section returned the flow velocity for each frequency inputted. The data were collected and post-processed with MATLAB®, returning the curve shown below.

Figure 3.10: Calibration curve of the TV-60 wind tunnel.

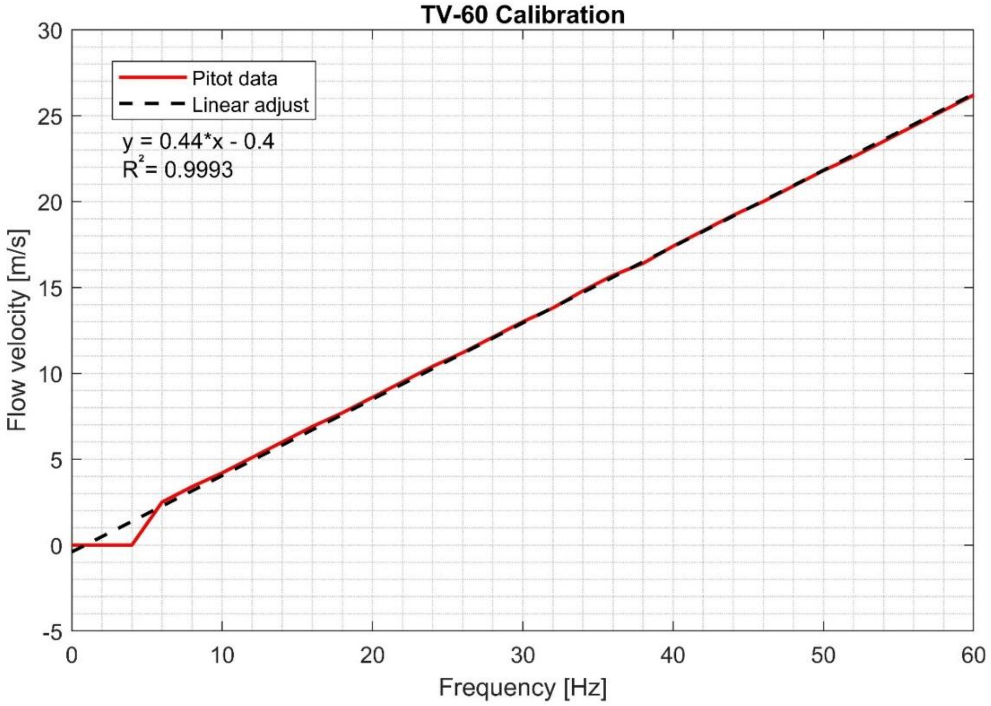

Source: Own authorship.

The data acquisition during this procedure showed that at a frequency of 46 hertz, the flow is at the speed of 20 meters per second. This is an important information, for the standard flow velocity established to perform the experiments is 20 meters per second.

3.4.2. Model construction

The physical model of the aircraft was fabricated with 3D printing. The original concept was reduced in a scale factor of 1:27, so the wingspan of the model would be approximately 40 centimeters and present a good fit inside the test section of the tunnel.

Nine parts of the model were printed separately and assembled later, with aid of guiding pins: two wings, four supports with two rotors each, two parts of the fuselage (front and back) and one structure integrating the empennages and the remaining supports. The equipment used to print those parts was the 3D printer Makerbot Replicator Z18, and the whole process took about 4 days to be completed. The total cost of the material used in this creation was around R$ 160,00.

The front section can be removed and the whole body presented a hollow inside to fit the pressure probes. A hole was positioned below the fuselage, at the gravity center position, so the support rod of the aerodynamic balance could be fixed in the model.

Whenever the model was prepared for an experiment, the halves were joined and fixed in place with duct tape. The groove between them was filled with modelling clay, so the surface would be as smooth as possible.

Figure 3.11: Printed model of the aircraft.

Source: Own authorship.

Little holes were made following a center line above the fuselage, were the pressure probes would be fixed. Due to construction limitations, the first two holes were discarded, leaving eight pressure probes above the fuselage, spaced 10 millimeters apart, starting at the third visible hole.

Lateral holes were made to shelter the last two pressure probes, one in each side of the fuselage.

Figure 3.12: Top pressure probes over the fuselage.

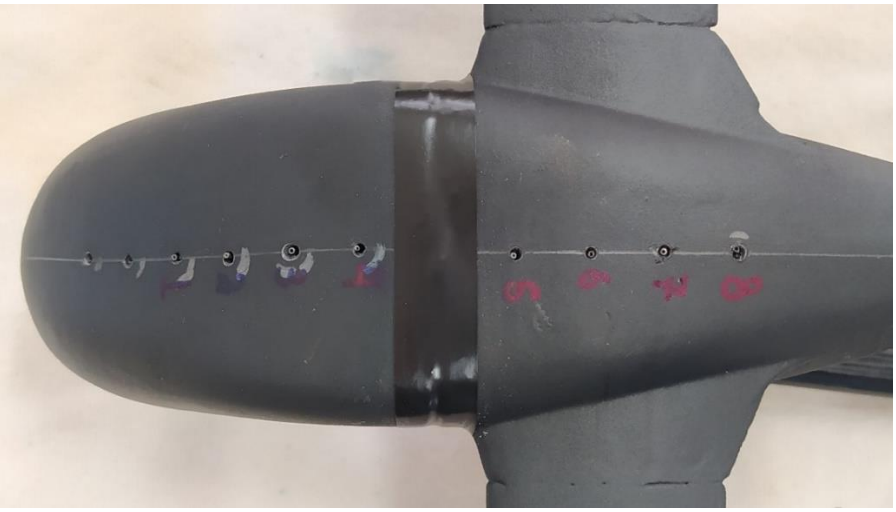

Source: Own authorship.

Figure 3.13: Lateral pressure probe positioned at the right side of the fuselage.

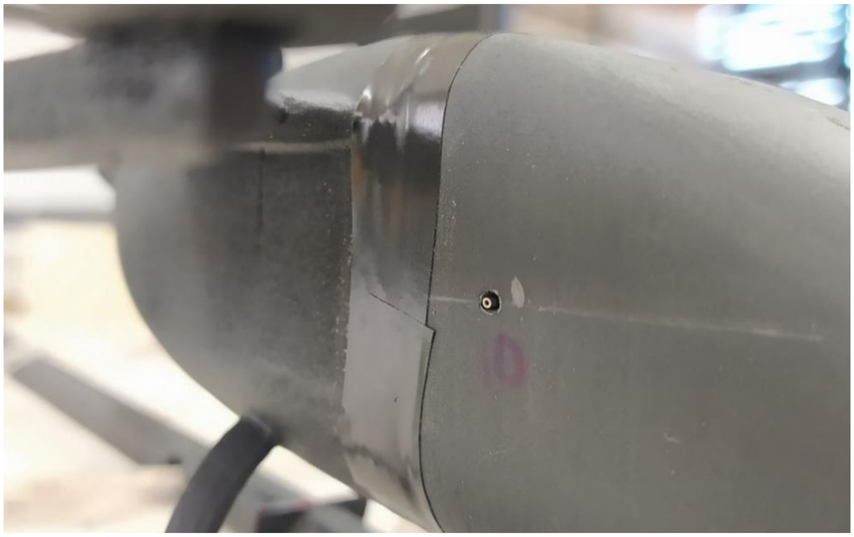

Source: Own authorship.

3.4.3. Pressure probes

The first experiment aimed to obtain the pressure difference between each point over the fuselage and a reference static pressure collected at the inside of the test section. Each pressure probe was connected to a silicon hose that led to a multi-port simultaneous pressure scanning system model AA-TVCR2® with 64 channels, along with a pressure module for a multi-hole pitot system (Aeroprobe®). Steady state pressure measurements were acquired with 0,50% of accuracy in the pressure channels, with range of 2000 Pa. The hoses passed through the inside of a support rod designed to hold the model inside the test section of the tunnel.

In addition to the fixed probes, a mobile probe numbered “11” was fixed in different positions in each round of data acquisition, always facing the flow directly.

Figure 3.14: Model inside the test section, with the hoses passing through the rod and the pressure transducer below the section.

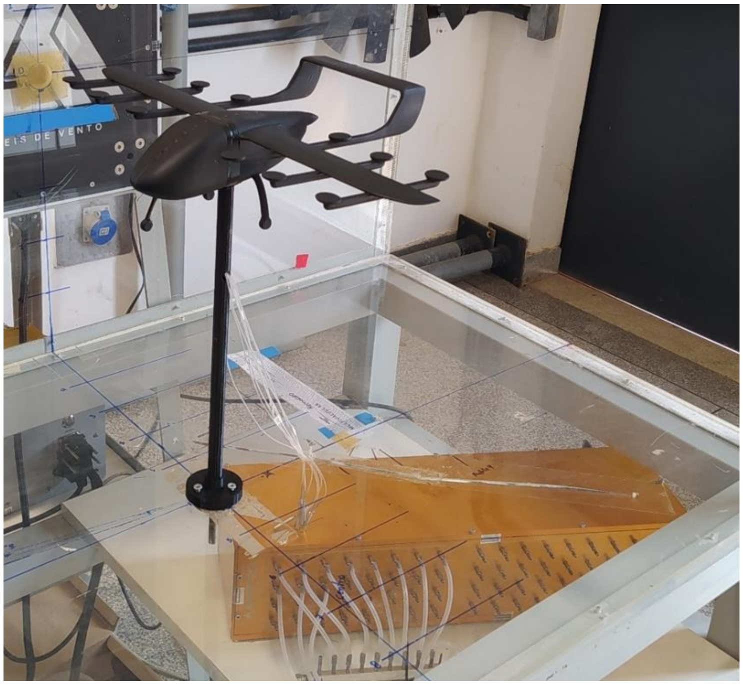

Source: Own authorship.

After the model positioning, the flow velocity was set to 20 meters per second in each round, and for each position of the eleventh probe the acquisition was conducted three times in the same conditions. For each round, the software collected the pressure values of every probe for 60 seconds, at a rate of one measurement each 0,5 seconds.

The lateral probes (ninth and tenth, respectively), were useful for guaranteeing the longitudinal orientation of the model. That way, they were expected to return similar pressure values, so it is possible to affirm that the model was oriented as intended in relation to the flow.

As mentioned, the eleventh probe was positioned in different locations for each round of tests, being them:

1) Left side of the nose gear;
2) Center of the horizontal stabilizer, over the surface;
3) Over the junction line of the left wing, between the fuselage and the first rotor support;
4) Over the back horizontal left rotor, near the fuselage;
5) Over the left wingtip.

Figure 3.15: First position of the eleventh probe.

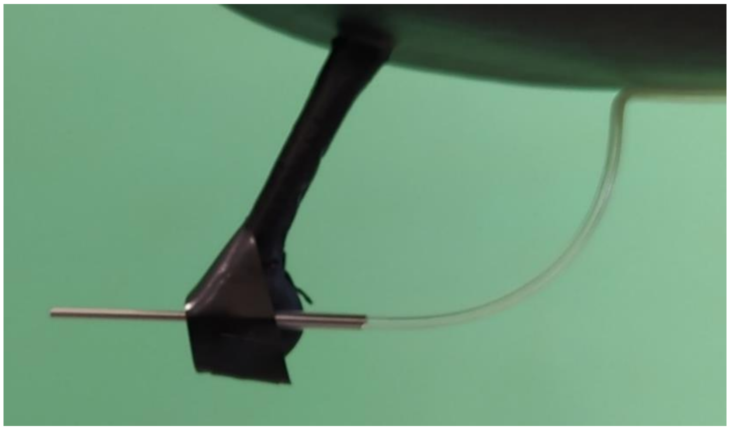

Source: Own authorship.

Figure 3.16: Second position of the eleventh probe.

Source: Own authorship.

Figure 3.17: Third position of the eleventh probe.

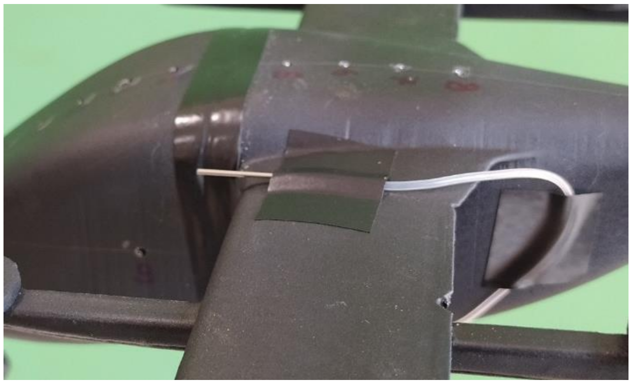

Source: Own authorship.

Figure 3.18: Fourth position of the eleventh probe.

Source: Own authorship.

Figure 3.19: Fifth position of the eleventh probe.

Source: Own authorship.

It is necessary to emphasize that, during the data acquisition, it was noted that the first pressure probe, nearest the aircraft nose, was probably compromised. This conclusion was drawn due to discrepant data returned by the software for this point.

Next image shows the horizontal distance of each probe position, relative to the nose of the aircraft. In this picture, it is also possible to observe the nomenclature applied to identify these probes. The probe P1 is the first working probe, that is, the real model has two other probes ahead of that, which weren't working and therefore weren't considered for the experimental tests.

Figure 3.20: Fuselage pressure probes position and identification [mm].

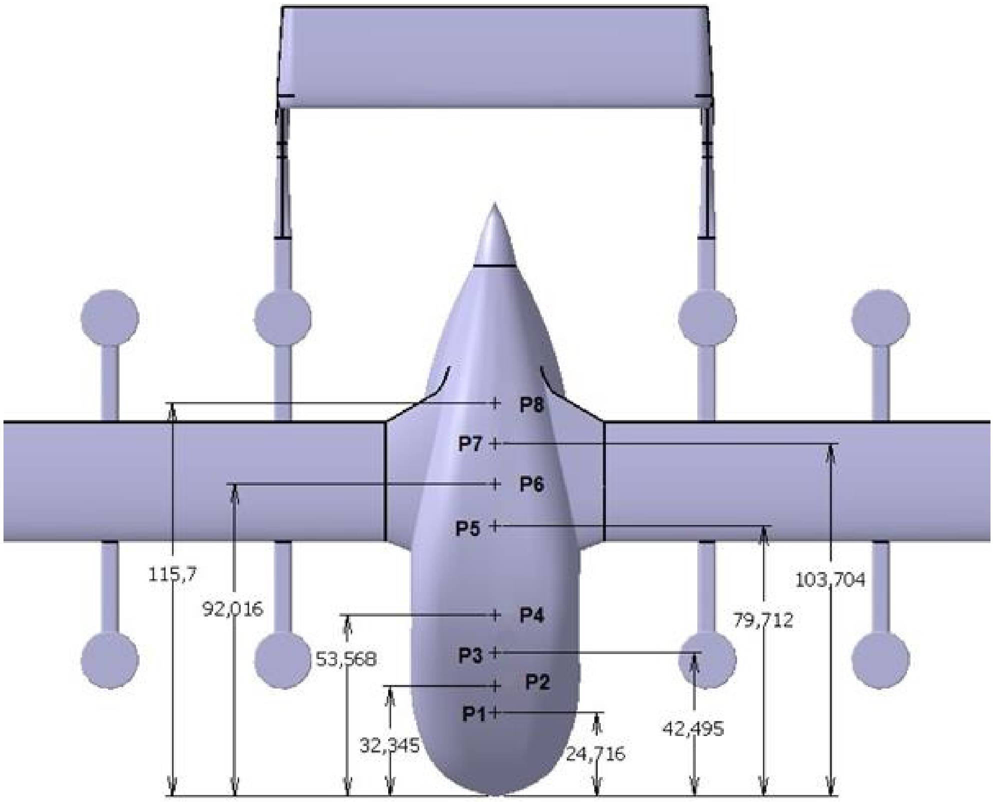

Source: Own authorship.

3.4.4. Pressure rake

The second experiment consisted in positioning a rake that holds 13 pressure probes vertically, in order to obtain the velocity profile of the flow in different positions. These probes will be from now on denominated P1 to P13, counted from top to bottom. The hoses of each pressure probe were connected to the same pressure transducer to return values of the pressure difference between the probes and the static pressure reference.

The horizontal distance was set to be 11.6 centimeters between the trailing edge of the horizontal stabilizer and the nozzle of the pressure probes. That is the length of the model divided by 2. The vertical position was also fixed, in a way that the seventh and central pressure probe was aligned to the trailing edge of the horizontal stabilizer.

The lateral position of the rake was modified for each round of acquisitions, following the order:

1) Centralized;
2) Behind the left wing, between the empennage and the middle-wing rotors;
3) Behind the left wing, between the middle-wing and the wingtip rotors.

Figure 3.21: Rake positioned right behind the model.

Source: Own authorship.

During the initial tests, it was noted that the fourth probe (counting from top to bottom) was also compromised. The solution was to add a replace probe at the other side of the rake, matching the fourth probe position. A new hose was connected to it and the test showed coherent values after this change.

The sequence of images below shows the distances (in millimeters) involved in the rake experiment, as well as the three tested lateral positions mentioned before. The black line represents the rake, with the 13 equidistant probes marked on it.

Figure 3.22: Rake probes, nomenclature and distances involved [mm].

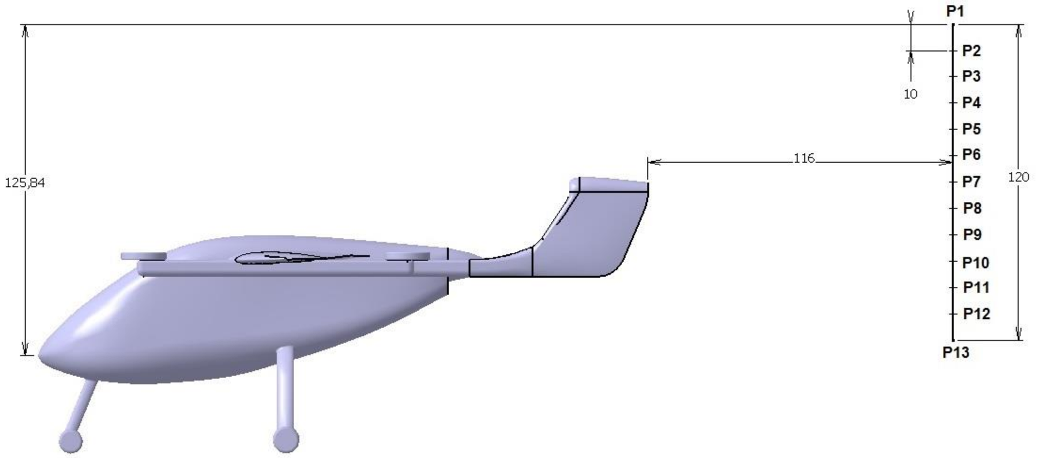

Source: Own authorship.

Figure 3.23: The three tested lateral positions of the rake [mm].

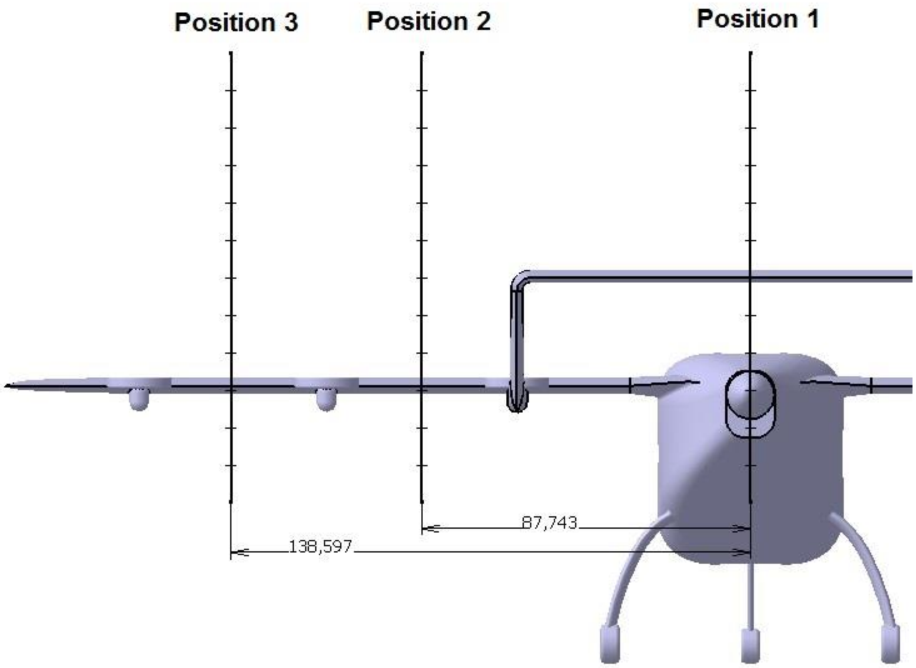

Source: Own authorship.

3.4.5. Aerodynamic drag coefficient

At this phase, the goal was to measure the aerodynamic drag of the model submitted to the same 20 meters per second flow. In order to do that, a 3-component aerodynamic balance (AA-TVAB1®) located beside the test section of the tunnel was used.

The model would be fixed in a rod that connected the bottom of the aircraft to the balance. This way, the model was positioned with a 90 degrees rotation angle inside the section. A consequence of this setup was the impossibility of measuring the lift force, due to equipment limitations.

Figure 3.24: Model positioning for the aerodynamic drag evaluation.

Source: Own authorship.

Since only the drag force would be acquired, the proposal was to measure the drag force with just the rod and after it, the drag force of the full set. Hence, the drag force could be corrected at the end, obtaining the just drag force of the model.

Therefore, three rounds of tests were conducted for three different conditions:

1) Just the rod;
2) Rod + Model with 0 degrees between longitudinal axis and flow direction;
3) Rod + Model with 6 degrees between longitudinal axis and flow direction.

Figure 3.25: The third configuration, where the model is positioned forming a 6-degree angle between the longitudinal axis and the flow direction.

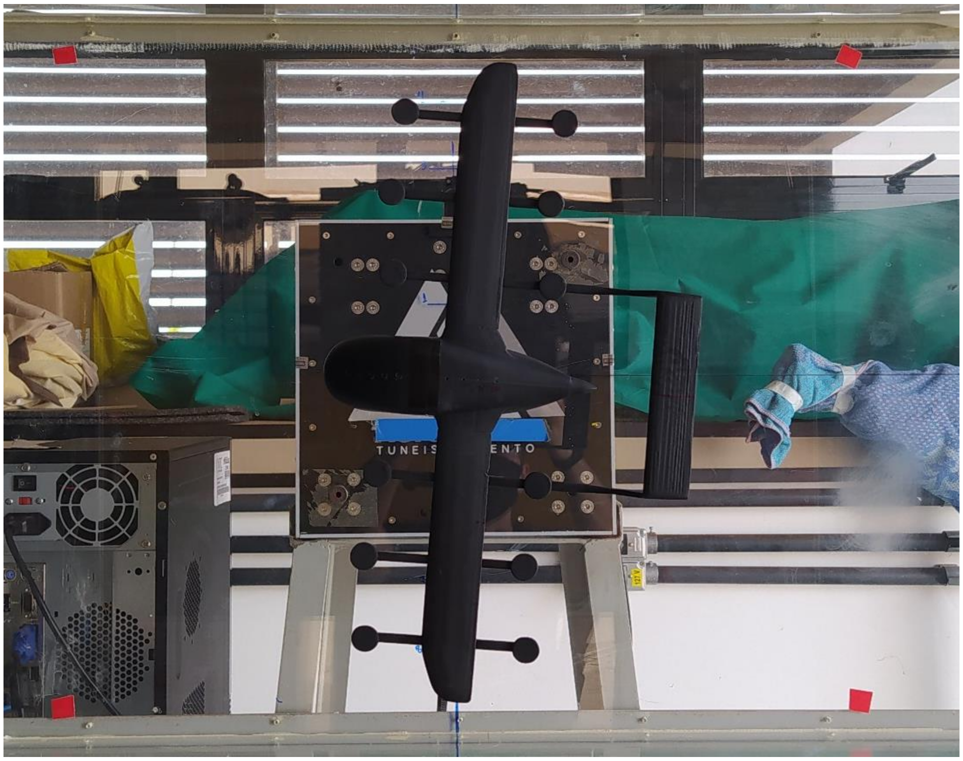

Source: Own authorship.

3.4.6. Flow visualization

The last experiment involving the aircraft model was a flow visualization, where the model was positioned inside the test section of the wind tunnel and covered with a special pigment, named China Clay (Barlow et al, 1999). After receiving the pigment cover, the model was submited to a 20 meters per second flow and left to it until the paint dries. This process left a visual mark of the flow behavior over the surfaces of the model, which will be presented in Chapter IV.

3.5. Numerical analysis

This section aims to present the settings of the numerical analysis implemented in this work. Here are explained the computational domain discretized for the process and other important information relative to the numerical simulation procedure.

3.5.1. Computational domain

The computational domain was defined for half-model, saving computational effort. The domain frontiers were defined in a distance such that the flow field around the body would suffer no influence of the borders.

All the distances used to define the dimensions of the domain were based on the actual length of the scale model, which is L = 231.91 mm. Basically, the domain consists of a quarter sphere ahead of the model, with a half cylinder developed backwards, starting from the semi-circle face of the quarter sphere. It all becomes clearer in Figure 3.26.

Figure 3.26: Three views with dimensions of the computational domain. This representation is out of scale for better visualization.

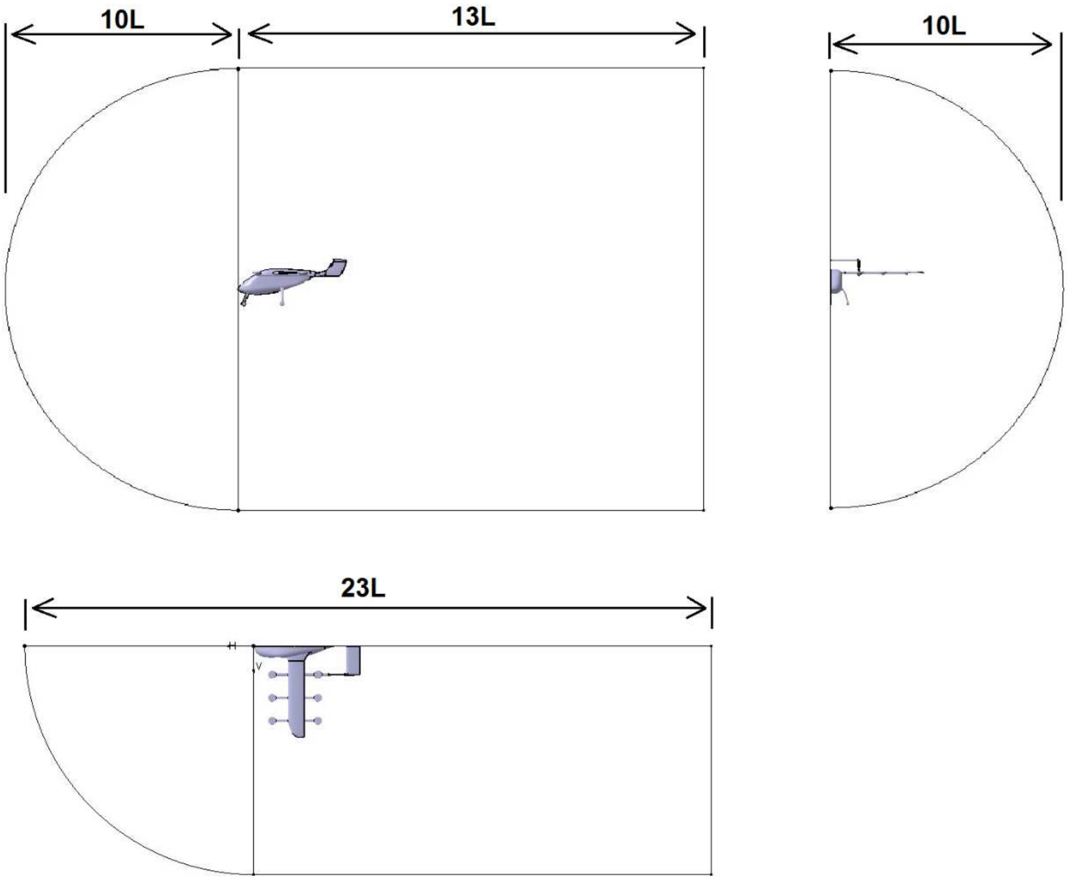

Source: Own authorship.

3.5.2. Mesh

The proposed configuration for the mesh is based in some main structures, which are:

1) The far field;
2) The near field;
3) The inflation;
4) The surface of the aircraft; and
5) Refinement spheres.

The near field domain consists of a geometric boundary involving the aircraft, aiming to provide a smooth transition of the mesh size, from the far field to the surface of the model.

The inflation is made of layers immediately above the surface of the model. The wall spacing between the elements of the inflation was computed through the following parameters:

Table 3.2: Reference parameters for inflation wall spacing calculation.

Freestream Velocity (U_∞) [m/s]	Freestream Density (ρ) [kg/m^3]	Dynamic Viscosity (μ) [kg/m.s]	Reference Length (L) [m]	Y^+
20.0	1.154	1.899×10^{-5}	0.232	30.0

Source: Own authorship.

This numbers resulted in a wall spacing $\Delta S = 0.53051$ mm. Due to the characteristics of the CAD model, which includes small ratio curvatures and other features difficult to mesh, the number of piled layers composing the inflation was maintained in a total of six.

The surface of the aircraft was always slightly more refined than the near field, so it is intended to reproduce the effects of the pressure gradient and wall shear observed experimentally.

In order to maintain the orthogonal quality and the skewness of the mesh elements within an acceptable margin (above 0.1 and below 0.95, respectively), some regions of the model needed extra-refining. This way, refinement spheres were strategically positioned to contain those problematic spots and hold those parameters in acceptable values.

A coherent analysis of the flow behavior related to the aircraft model requires a mesh that is properly refined. Ideally, a more refined mesh will undoubtedly provide better results, but for that there is a high price in terms of computational cost. This way, it is necessary to achieve a mesh considered both sufficient to provide a coherent result and viable regarding the computational effort.

With that in mind, two meshes were developed starting from an original 6.4 million elements mesh. The characteristics of each one are related in Table 3.3. Below it, a sequence of three images shows how Mesh 2 looks like. The CFD calculations are done in a workstation with an Intel Core i7-3930K (3.20 GHz) processor with twelve cores (six physical) and 48.0 GB RAM memory.

Table 3.3: Studied mesh configurations.

Mesh	Refining Factor	Number of Elements	Elapsed Time [min]
Mesh 1	1.183216	2,698,745	161
Mesh 2	1	6,422,799	406
Mesh 3	0.707107	10,100,767	989

Source: Own authorship.

Figure 3.27: A close view of the mesh.

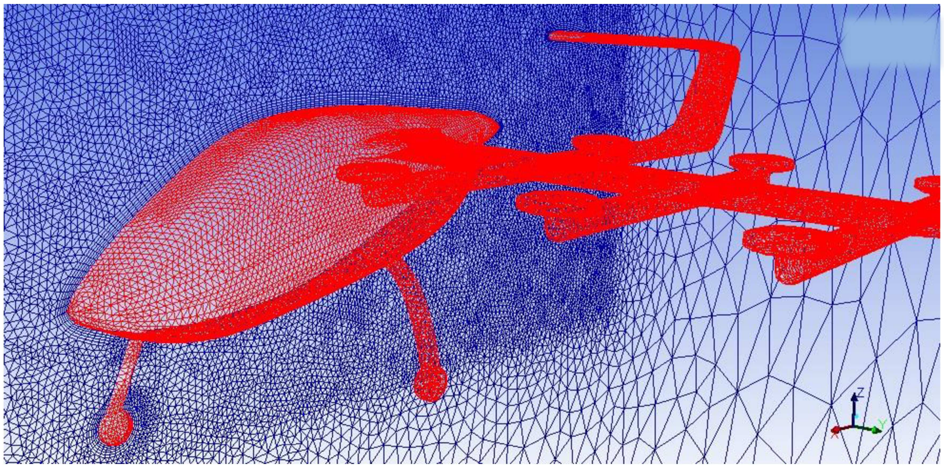

Source: Own authorship

Figure 3.28: A close view of the mesh around engine supports.

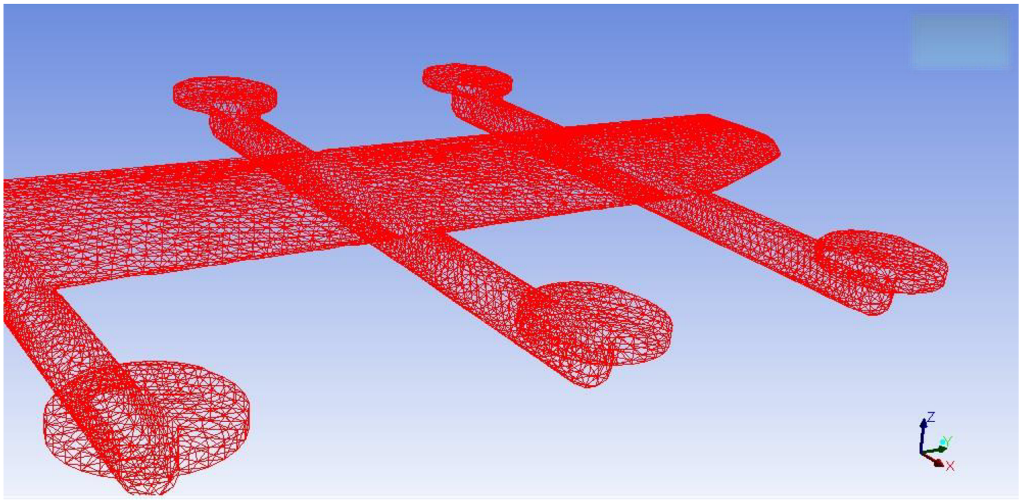

Source: Own authorship

Figure 3.29: A highlight of the inflation layer intersected with the symmetry plane.

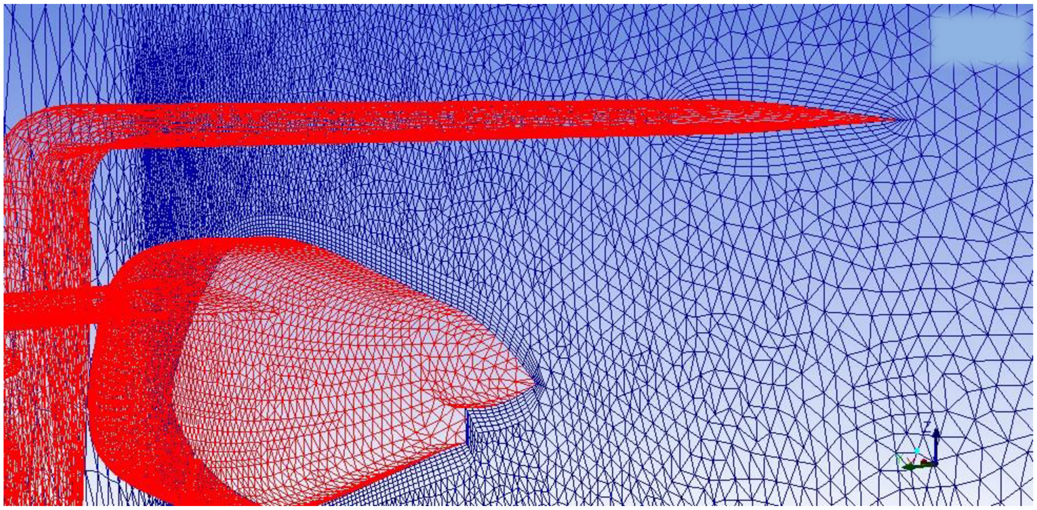

Source: Own authorship

3.5.3. *Turbulence model and reference conditions*

The implemented turbulence model was the RANS Two-Equation Realizable k-ε. It consists in a two-equation model that gives a general description of turbulence by means of partial differential equations.

This choice is justified by the fact that the flow will not suffer abrupt changes in the pressure coefficient and there is no heat injection in the domain. As stated by Baglietto (2016), *“[Realizable k -epsilon] is the default recommendation in mainstream commercial packages, therefore represents the most proven, well-quantified and widely-documented of all closures. The model has improved performance for planar surfaces, round jets, rotation, recirculation and streamline curvature.*”

The reference conditions used in the simulations are shown in Table 3.4.

Table 3.4: Reference conditions for the simulations.

Property	Representation	Value
Geometry	S/2	0.003 m^2
	L	0.232 m
Fluid	ρ_∞	1.154 kg/m^3
	μ_∞	1.899 x 10^{-5} kg/m.s
Flow	U_∞	20.0 m/s
	Re	2.820 x 10^5

Source: Own authorship.

CHAPTER IV

Results and Discussions

This section is dedicated to the presentation and discussion of both experimental and numerical results.

4.1. Mesh convergence

The first simulations aimed to define which one of the three developed meshes was more adequate to this study. The main factors, as it was stated, were computational cost and reliability.

The computed results used to this comparison were the drag and lift coefficient conversion, after 2000 iterations. The last values of each simulation were obtained and compared to return a conclusion above the mesh convergence, which is shown in Table 4.1.

Table 4.1: Mesh convergence data.

Property	Mesh 1	Mesh 2	Mesh 3	Relative deviation Mesh 1 to 2	Relative deviation Mesh 2 to 3
C_D	0.264	0.247	0.243	6.8%	1.4%
C_L	0.081	0.089	0.089	10.1%	0.4%

Source: Own authorship

The results show a small deviation from Mesh 2 to Mesh 3. From this, it is possible to conclude that Mesh 2 fulfill the reliability criteria, in addition to be more viable from the point of view of computational effort, as observed in Table 3.3. The next analysis will thus be based in results obtained from simulations using Mesh 2.

4.2. Experimental Results

This section is dedicated to present the experimental results of this work, which will later be confronted with the numerical results obtained through the CFD simulations.

4.2.1. Pressure probes

The acquired values of delta pressure in each probe, for each round of experiments, were processed to return the mean values in terms of pressure coefficient. The used equation for this procedure is shown below:

$$C_P = \frac{\Delta P}{\frac{1}{2}\rho_\infty V_\infty^2} \tag{4.1}$$

Where:

- ΔP is the difference between the pressure at the point of evaluation and the pressure in the freestream;
- ρ_∞ is the fluid density, which was considered 1.15308 kg/m^3 based on local conditions at the moment;
- V_∞ is the freestream velocity of the fluid in meters per second.

The C_P values referent to each pressure probe are presented in Table 4.2. It is interesting to recall that the 11th probe (P11) was the only floating one, so there will be a separated table to account those results. Also, the probes P9 and P10 are located on both sides of the fuselage, hence their provided data are useful to verify the alignment of the model inside the wind tunnel.

Table 4.2: Pressure coefficient values for each probe.

Probe	P1	P2	P3	P4	P5	P6	P7	P8	P9	P10
Delta P [Pa]	-16.0	-86.2	-118.2	-125.5	-127.3	-116.7	-96.2	-62.9	-47.6	-46.6
C_P	-0.07	-0.37	-0.51	-0.54	-0.55	-0.51	-0.42	-0.27	-0.21	-0.20

Source: Own authorship.

Table 4.3: Pressure coefficient values for probe 11.

Position of the 11th probe	Nose gear	Horizontal tail	Wing junction	Rotor	Wingtip
C_P	0.95	0.96	0.94	0.86	0.95

Source: Own authorship.

The following graphic relates the information presented in Table 4.2 for the probes located over the fuselage, which are from P1 to P8.

Figure 4.1: Experimental C_P values for each probe, from P1 to P8

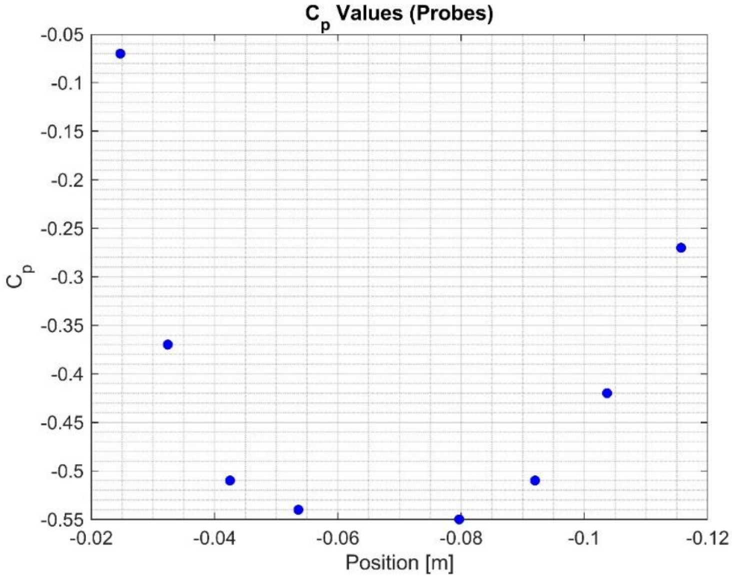

Source: Own authorship

4.2.2. Pressure rake

For the pressure rake experiment, the values of delta pressure for each round were also computed. The rounds of experiments returned mean values, which were useful to calculate the flow velocity at each probe, with aid of Bernoulli’s Equation, shown below.

$$\Delta P = p_t - p_s = \frac{\rho V^2}{2} \tag{4.2}$$

Where:

- ΔP is the difference between the total pressure p_t and the static pressure p_s;
- ρ is the fluid density, which was considered 1.15308 kg/m3 based on local conditions at the moment;
- V is the freestream velocity of the fluid in meters per second.

Thus, the velocity values for each probe (from P1 to P13), in each position of the rake, are presented in Tables 4.4 and 4.5.

Table 4.4: Flow velocity in each probe [m/s], experimentally obtained (Part 1).

Rake position	P1	P2	P3	P4	P5	P6
Behind horizontal tail	19.3	19.3	19.3	19.3	19.2	19.3
Behind wing (Near the fuselage)	19.2	19.1	19.2	19.2	19.1	19.1
Behind wing (Far from the fuselage)	19.3	19.2	19.3	19.3	19.2	19.2

Source: Own authorship.

Table 4.5: Flow velocity in each probe [m/s], experimentally obtained (Part 2).

Rake position	P7	P8	P9	P10	P11	P12	P13
Behind horizontal tail	18.5	19.0	17.0	16.4	16.8	17.4	16.7
Behind wing (Near the fuselage)	19.2	18.5	18.1	18.7	18.8	19.2	19.2
Behind wing (Far from the fuselage)	19.0	18.0	18.3	19.1	18.9	19.2	19.3

Source: Own authorship.

For each position of the rake, a graphic was produced to make the data above clearer. They are shown in the next three figures below.

Figure 4.2: Flow velocity for the first rake position, experimentally obtained.

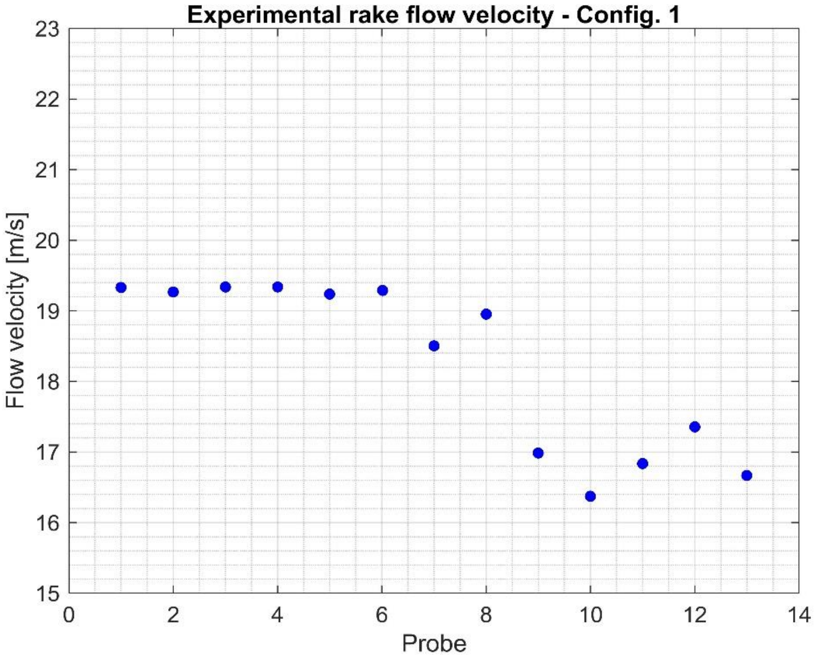

Source: Own authorship.

Figure 4.3: Flow velocity for the second rake position, experimentally obtained.

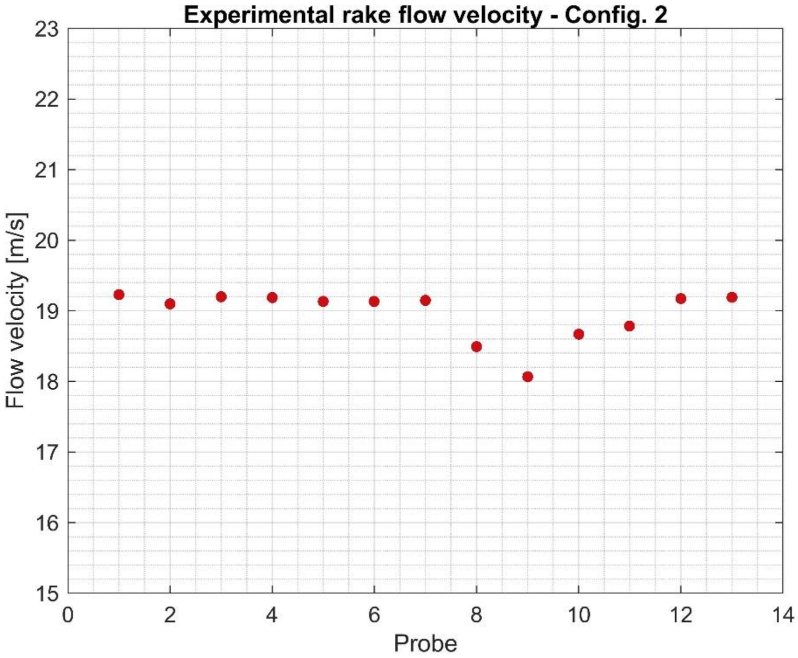

Source: Own authorship.

Figure 4.4: Flow velocity for the third rake position, experimentally obtained.

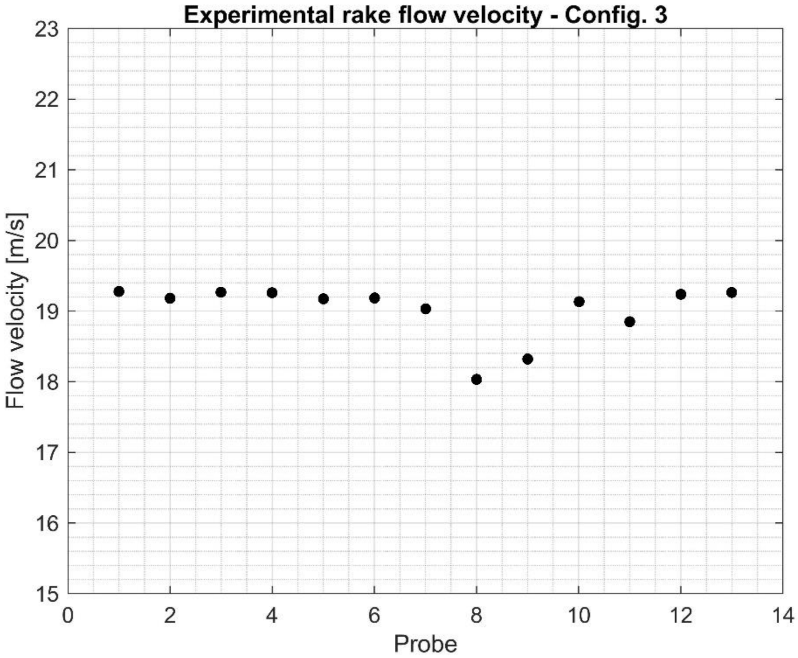

Source: Own authorship.

4.2.3. Aerodynamic drag coefficient

For the experiments involving the aerodynamic balance, each one of the mentioned configurations were tested, returning values in terms of kilogram-force. These values were used to obtain the drag coefficient for each configuration. Three rounds of experiments were performed for each setup and in each round, ten sample values were collected, so at the end it was possible to calculate a mean result.

The drag coefficient was obtained by the following equation:

$$C_D = \frac{D}{\rho_\infty \, A \, V_\infty^2/2} \tag{4.3}$$

Where:

- D is the drag component in Newtons;
- ρ_∞ is the fluid density, which assumed different values based on local conditions at the moment;
- A is the reference area, which was considered as 0.006 m^2;
- V_∞ is the freestream velocity of the fluid in meters per second.

The values of C_D obtained for each configuration are shown in Table 4.6 below.

Table 4.6: CD values for each configuration.

Setup	Flow velocity [m/s]	Temperature [°C]	Density [kg/m^3]	Mean C_D
Isolated rod	20.0	34	1.149	0.469
Rod + Model	20.1	35	1.146	0.750
Rod + Model (6 deg. drift)	20.1	35	1.146	1.100

Source: Own authorship

A simple subtraction shows the approximate obtained drag coefficient referent to the model alone, for the flow-aligned condition: $C_D = 0.281$

4.2.4. Flow visualization

The procedure was performed three times, and the images were registred for further comparison with the numerical simulation. One of these pictures is shown below.

Figure 4.5: Third result of the flow visualization over the wing.

Source: Own authorship.

4.3. Numerical results

This section will bring the numerical results of the CFD simulations, referring to the manipulations of Mesh 2 inside the computational environment. The results are intentionally disposed in the same order of the experimental data, for comparison reasons.

4.3.1. Pressure probes

The following graphic shows the data acquired by post-processing the CFD results, referring to the pressure profile above the fuselage in terms of pressure coefficient. The reference line matches the symmetry line of the model, going from the fuselage apex, which is the origin, in direction to the spinner behind, passing through the points where are located the pressure probes in the real model.

Figure 4.6: Pressure profile over the fuselage, numerically obtained.

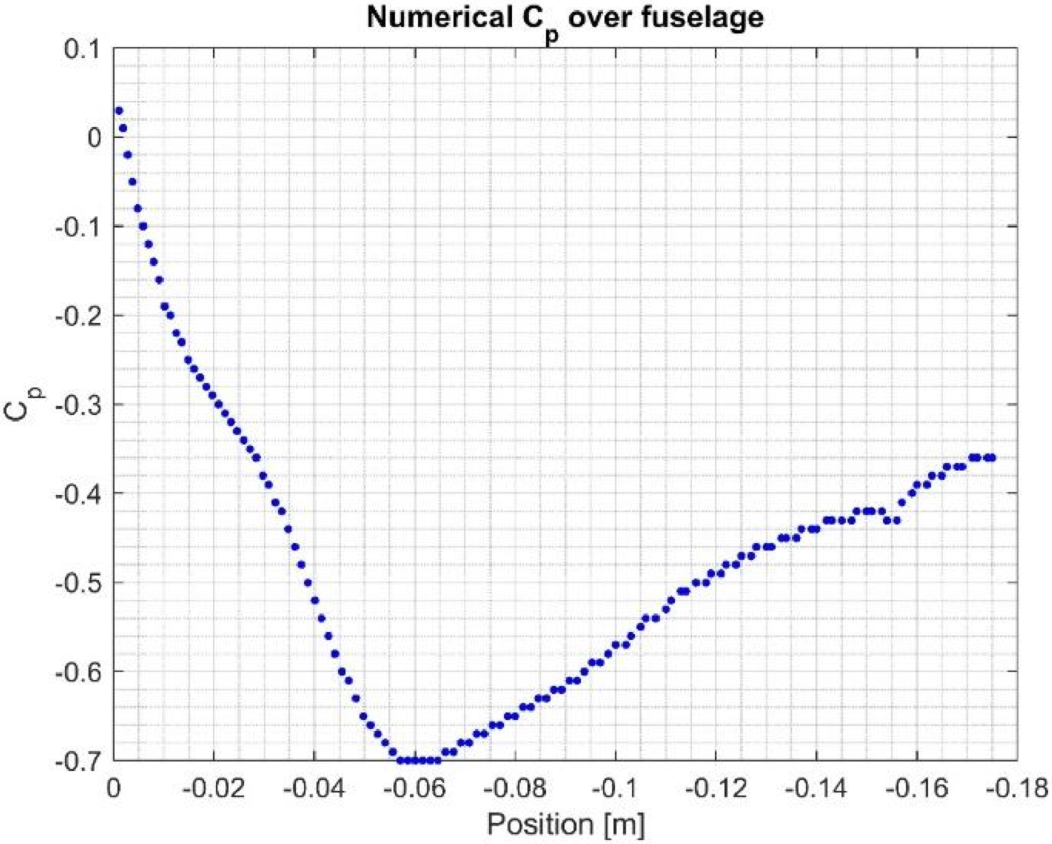

Source: Own authorship.

The behavior of the pressure coefficient curve above can be explained by the decay of pressure and the subsequent recovery over the fuselage. That is, it is very similar to the C_p values over an airfoil, once that the fuselage has a similar profile.

Since the horizontal position of each pressure probe is known (Figure 3.20), it is possible to select only the referenced ones from the simulation and compare their values with the ones shown in Figure 4.1. This comparison is presented below.

Figure 4.7. Comparison between experimental and numerical pressure coefficients.

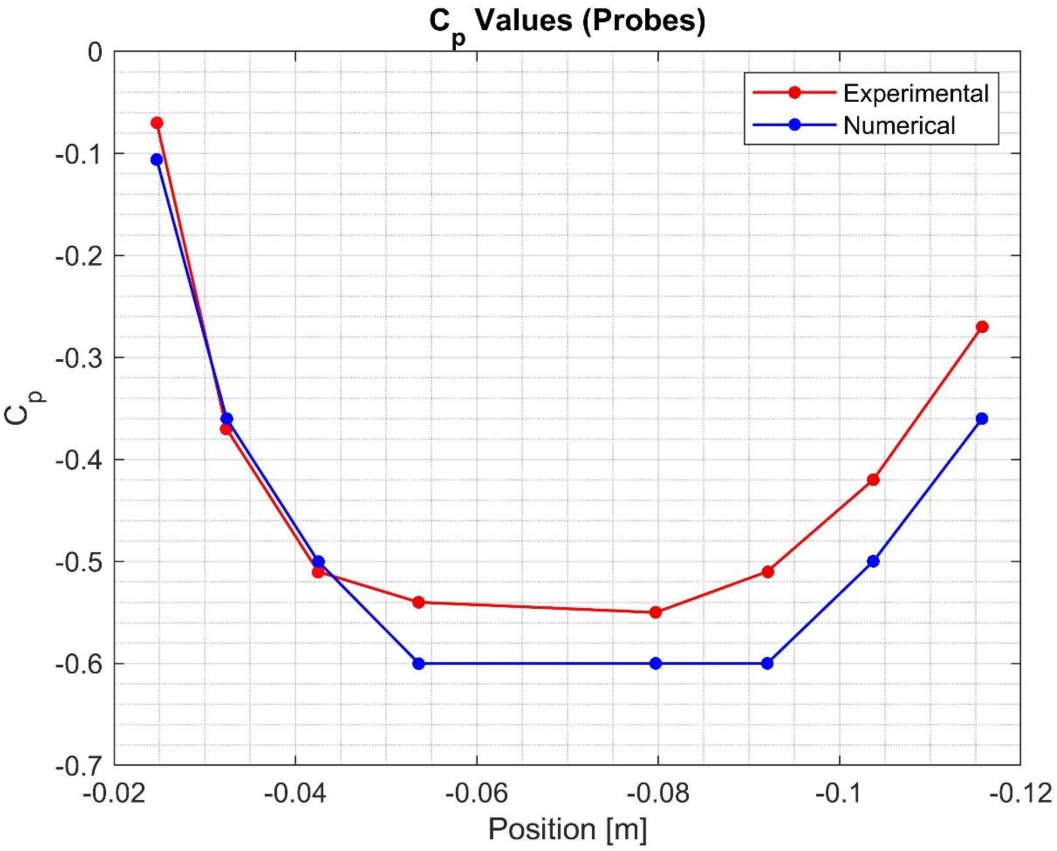

Source: Own authorship.

It is clearly visible that both numerical and experimental results follow the same pattern. Some points have higher deviations than others, like the last pair of values, which show a relative deviation of 25% between each other. Nevertheless, the differences observed between each value are expected and the overall result is quite satisfactory.

The notable reduced size of the model made it difficult to set all the probes with great quality, not allowing a good alignment between the probes and the model surface, making the instrumentation and measuring not ideal. Also, the results could be improved by an upgrade of numerical settings.

4.3.2. Pressure rake

With the aid of a virtual rake inserted in the CFD post-processing environment, it was possible to acquire velocity data at the same positions implemented in the experimental analysis. The results are shown at the identical tables disposed below.

Table 4.7: Flow velocity in each probe [m/s], numerically obtained (Part 1).

Rake position	P1	P2	P3	P4	P5	P6
Behind horizontal tail	19.2	18.7	18.2	18.0	17.9	18.3
Behind wing (Near the fuselage)	19.9	19.8	19.6	19.5	19.6	19.7
Behind wing (Far from the fuselage)	19.8	19.7	19.6	19.6	19.7	19.8

Source: Own authorship.

Table 4.8: Flow velocity in each probe [m/s], numerically obtained (Part 2).

Rake position	P7	P8	P9	P10	P11	P12	P13
Behind horizontal tail	18.8	19.4	19.8	19.9	20.0	20.0	20.0
Behind wing (Near the fuselage)	19.9	19.9	20.0	20.0	20.0	20.0	20.0
Behind wing (Far from the fuselage)	19.9	20.0	20.0	20.0	20.0	20.0	20.0

Source: Own authorship.

Just like the experimental data, three graphics were generated to make the results presented on Tables 4.7 and 4.8 clearer. They can be seen in the sequence.

Figure 4.8: Flow velocity for the first rake position, numerically obtained.

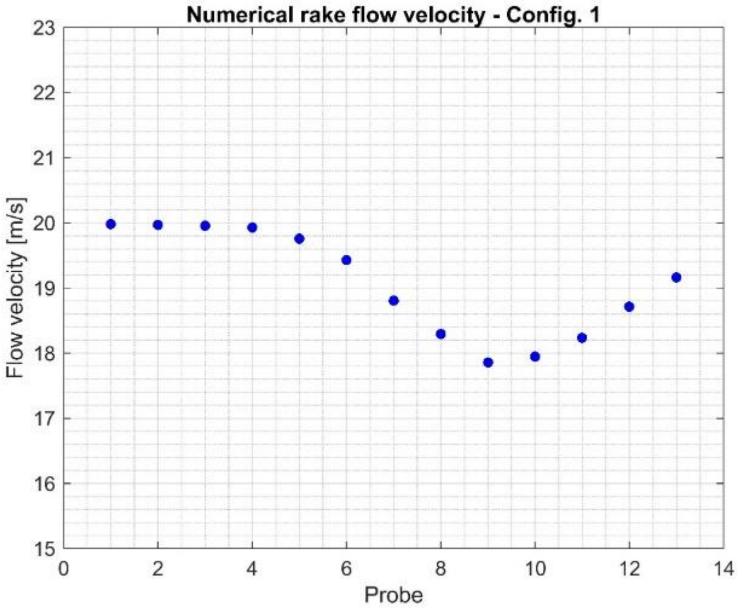

Source: Own authorship.

Figure 4.9: Flow velocity for the second rake position, numerically obtained.

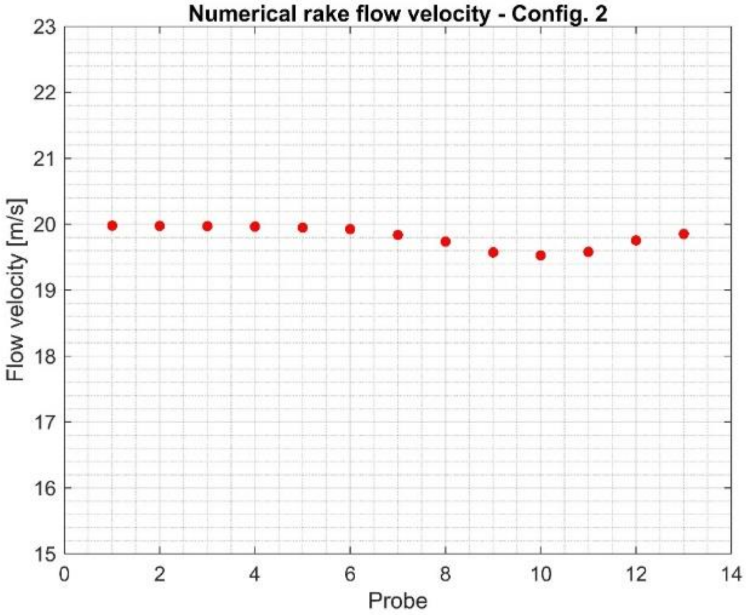

Source: Own authorship.

Figure 4.10: Flow velocity for the third rake position, numerically obtained.

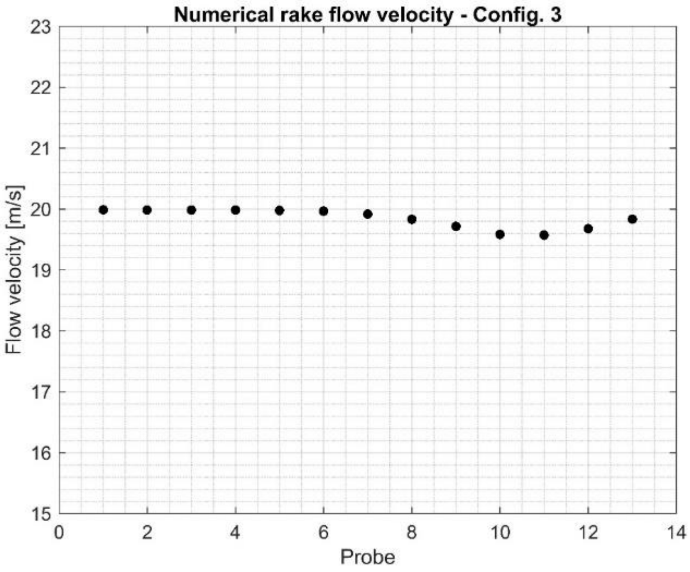

Source: Own authorship.

For comparison ends, the experimental and numerical results were overlapped in three graphics, one for each rake position. These graphics are shown below.

Figure 4.11: Flow velocity for the first rake position, comparison between experimental and numerical data.

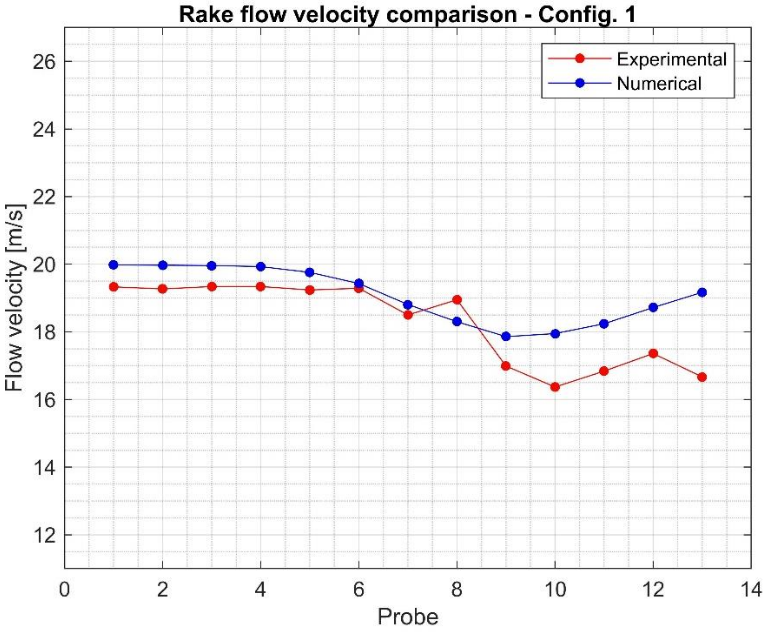

Source: Own authorship.

Figure 4.12: Flow velocity for the second rake position, comparison between experimental and numerical data.

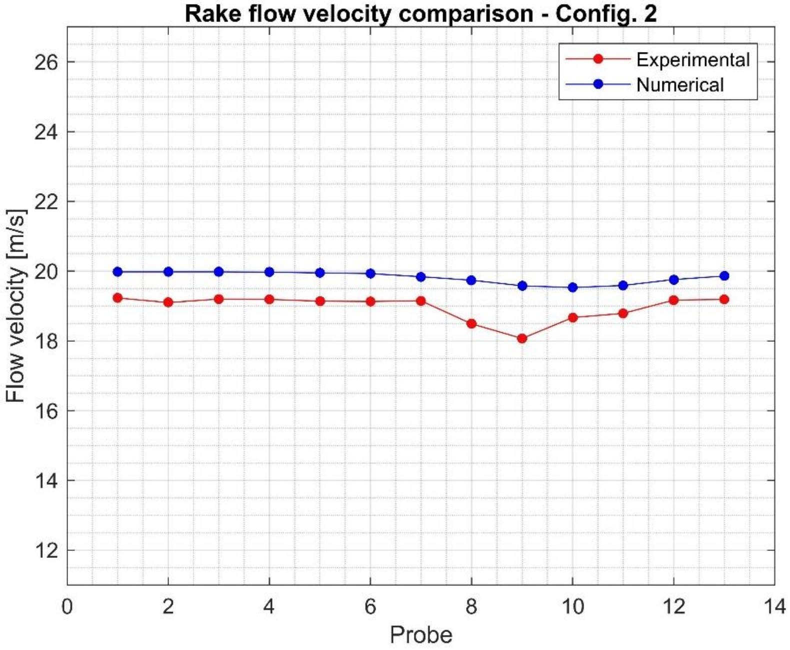

Source: Own authorship.

Figure 4.13: Flow velocity for the third rake position, comparison between experimental and numerical data.

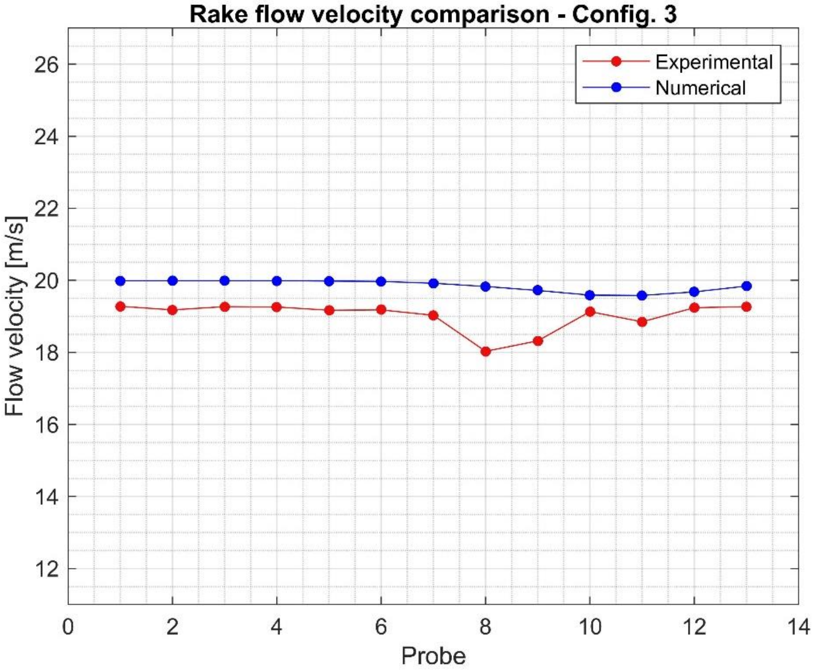

Source: Own authorship.

These charts show a notable difference between experimental and numerical results. For example, in Figure 4.11, it is visible that the experimental probe 8 reflects the horizontal stabilizer influence in flow velocity, a behavior that is not visible on numerical data.

Also, there is a general difference in achieved magnitudes of flow velocity for each probe position. It is necessary to state that the probes positioning on the physical model could be improved. As mentioned, the reduced size of the model made it difficult to set all the probes with great quality, affecting the results directly.

Despite that, the big scope brings a coherent form of the two curves for each case, demonstrating a consistent general behavior on both experimental and numerical analysis.

4.3.3. Aerodynamic balance

As mentioned in section 4.1, the last drag coefficient iteration value for Mesh 2 was $C_{D,num} = 0.247$. That number is reasonably close to the experimental result, which was $C_{D,exp} = 0.281$. This comparison shows that, although the numerical simulation deviates in some points from the experimental results, it represents the phenomena with notable fidelity.

This 12.1% deviation found between the two compared drag coefficients can be explained by many factors, some of them being the well reduced scale of the experimental model and the difficulty in meshing specific regions like the junction between rotors.

4.3.4. Flow visualization

The flow visualization experiment, which was done in the wind tunnel with China Clay, was reproduced in computational environment through the concept of wall shear. As it is shown in Figure 4.14, the flow behavior resembles the same characteristics observed in the wing when submitted to the experimental version of this test.

Figure 4.14: Fluid behavior over the wing, CFD (left) and China Clay (right).

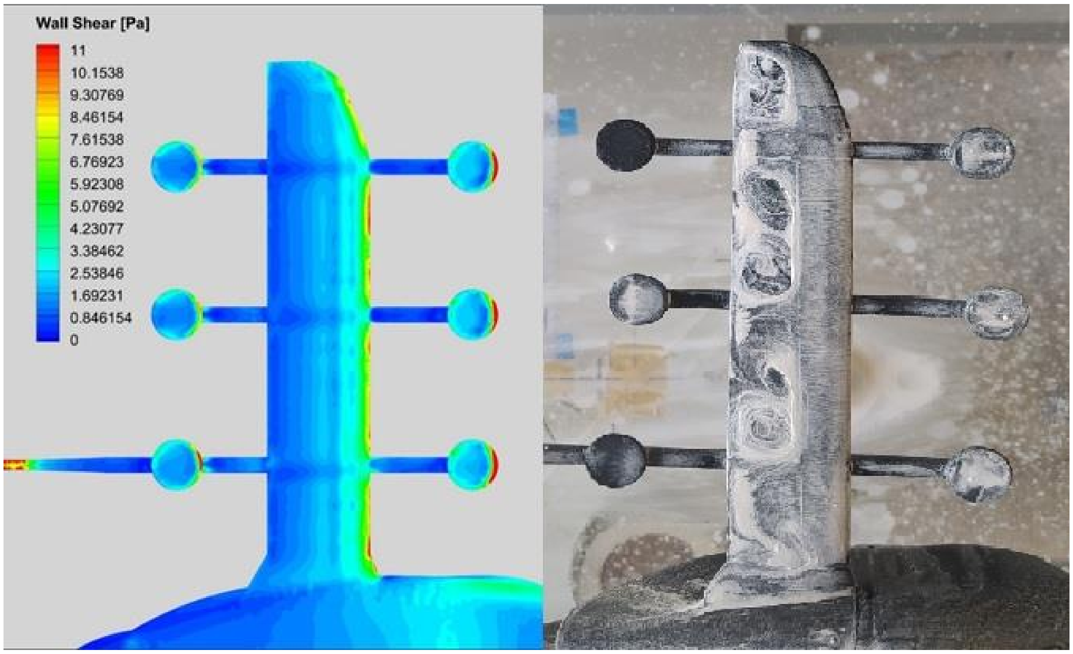

Source: Own authorship.

4.4. Future works

Thinking about future works in the eVTOLs field, there are some lines of improvement that can be developed using this work as a starting point. Modifications of the model geometry and scale can be implemented to validate experimental and numerical similarity observed here. A new concept can also be proposed, aiming to gather other advantageous characteristics for a more promising project.

Regarding the computational analysis, it is suggested for future works, related to this one, to develop a more detailed study about meshing and solver methods, searching for improvements in the results obtained by the presented means.

CHAPTER VI

Conclusion

An understanding of the most valuable and viable characteristics of the main current concepts was constructed, going through the main considerations regarding a vehicle of this kind, like mission profile, passenger safety, efficiency and real scenario applicability. Starting from that point a new design for an eVTOL was proposed, using CAD tools and real dimensions from an original concept.

A numerical and experimental study of the aerodynamics of an eVTOL concept was performed. Studied geometry was established on the dimensions of the most promising models in current development. The conceived model is composed by fillet surfaces, sharp edges and reduced structures. Numerical steady simulations (RANS) were performed on commercial software Ansys, specifically the Fluent tool, using two-equation realizable k-ε turbulence model; the tetrahedral mesh implemented on the solver has an average of 6 million elements. All simulations were prepared on an i7 processor with 12 cores, 48 GB of RAM. For wind-tunnel testing, model was 3D printed in 1:27 scale. On experimental procedures, qualitative (china clay visualization) and quantitative (pressure profiles and drag coefficient) were conducted, while on computational domain, the same conditions were reproduced to further comparison.

Because of the reduced size of the model, experimental setup had to discard the first two projected probes, for they would not return reliable data due to the insufficient room inside the fuselage to the hoses to transmit the pressure to the transducer. Also, one of the probes on the rake setup had to be replaced for being returning unreliable data, probably due to an obstruction. Despite these particularities, the experiments were well conducted and produced all the information this work required.

During the numerical process implemented by this work, the mesh construction was the most difficult step, thanks to the complexity of meshing some of the interfaces presented by the concept, specially the junction between rotor and support. It required local refinement and several tries until the mesh quality presented an acceptable level.

The results returned by both experimental and numerical processes had revealed some expected deviations, that can be attributed to environmental variations, impaired probe positioning due to the reduced scale of the model, and the necessity of a more elaborated CFD setup. Even with those differences, the studied phenomena could be observed in both experimental and numerical results. The pressure coefficient curve composed by the positioned probes follow the same pattern, as well as the rake pressure profile. Finally, the drag coefficient presented a notable proximity in both cases, confirming that the information obtained by the two methods are surely close to each other.

This work aims to be a starting point and a reference for general concepts and ideas regarding eVTOL projects and their aerodynamic study, and it is expected to be a starting point for other deepened studies that will take advantage of CFD modeling to enlighten the flight characteristics of this new modal of transportation.

REFERENCES

[1] Almeida, O., 2021. **The development of an experimental aerodynamics research center in Brazil**. International Journal of Advanced Engineering Research and Science, 8(3), pp.159-172. https://dx.doi.org/10.22161/ijaers.83.16

[2] **Archer Maker**. Available at: https://www.archer.com/maker. Access on July 29th, 2021.

[3] BACCHINI, Alessandro; CESTINO, Enrico. **Electric VTOL Configurations Comparison**. Aerospace, [S.L.], v. 6, n. 3, p. 26, February 28th, 2019. MDPI AG. http://dx.doi.org/10.3390/aerospace6030026.

[4] BALLI, Mehmet Efe. **eVTOL aircraft conceptual design and optimization**. 2019. 124 f. Dissertação (Master Degree) - Mechanical Engineer, Dipartimento di Meccanica, Politecnico di Milano, Milan, 2020.

[5] BARLOW, Jewel B.; RAE, William H.; POPE, Alan. **Low-speed wind tunnel testing.** John Wiley & Sons, 1999.

[6] CAMBRIDGE UNIVERSITY PRESS (ed.). **Cambridge Dictionary**. Available at: https://dictionary.cambridge.org/dictionary/english/. Access on August 19th, 2021.

[7] **City Airbus**. Available at: https://www.airbus.com/innovation/zero-emission/urban-air-mobility/cityairbus.html. Access on July 29th, 2021.

[8] **EHang**. Available at: https://www.ehang.com/ehangaav/. Access on July 26th, 2021.

[9] **Electric VTOL News**. Available at: https://evtol.news. Access on July 23th, 2021.

[10] ENCYCLOPAEDIA BRITANNICA (ed.). **VTOL Airplane**. Available at: https://www.britannica.com/technology/VTOL-airplane. Access on August 19th, 2021.

[11] HIGGINS, Ross J.; BARAKOS, George N.; SHAHPAR, Shahrokh; TRISTANTO, Indi. **A computational fluid dynamic acoustic investigation of a tiltwing eVTOL concept aircraft**. Aerospace Science and Technology, [S.L.], v. 11, April, 2021. Elsevier BV. http://dx.doi.org/10.1016/j.ast.2021.106571.

[12] LILIUM. Available at: https://lilium.com. Access on July 28th, 2021.

[13] LOPEZ, Diego; SHAHPAR, Shahrokh; TRISTANTO, Indi; MANOHAR, A.; FILLINGHAM, David. **Aerodynamic Optimization of an eVTOL Wing**. Researchgate, p. 1-4, out. 2019.

[14] NOE, Rain. **How Distributed Electric Propulsion Will Change the Way We Design Flying Vehicles**. 2015. Available at: https://www.core77.com/posts/36900/How-Distributed-Electric-Propulsion-Will-Change-the-Way-We-Design-Flying-Vehicles. Access on August 27th, 2021.

[15] NORRIS, Guy. **Catch an Air Taxi? Aviation Week Flies Joby's EVTOL Simulator**. 2020. Available at: https://aviationweek.com/aerospace/urban-unmanned-aviation/catch-air-taxi-aviation-week-flies-jobys-evtol-simulator. Access on August 8th, 2021.

[16] PICCININI, Riccardo; TUGNOLI, Matteo; ZANOTTI, Alex. **Numerical Investigation of the Rotor-Rotor Aerodynamic Interaction for eVTOL Aircraft Configurations**. Energies, [S.L.], v. 13, n. 22, November 17th, 2020. MDPI AG. http://dx.doi.org/10.3390/en13225995.

[17] **Popular Mechanics Magazine**. E. Ontario St.: Popular Mechanics Company, v. 111, n. 3, March 1959. Monthly.

[18] SIGLER, Dean. **Wisk Tests Cora in US, New Zealand**. 2020. Available at: http://cafe.foundation/blog/wisk-tests-cora-in-us-new-zealand/. Access in September 2nd, 2021.

[19] SILVA FILHO, Rogério Rodrigues da. **Análise Numérica das Características Aerodinâmicas de uma Asa de Baixo Alongamento com Propulsão Distribuída**. 2020. 149 p. Dissertation (Master Degree) – Mechanical Engineering, Escola de Engenharia, Universidade Federal de Minas Gerais, Belo Horizonte, 2020.

[20] SIMMONS, Benjamin M.; MURPHY, Patrick C.. **Wind Tunnel-Based Aerodynamic Model Identification for a Tilt-Wing, Distributed Electric Propulsion Aircraft**. Aiaa Scitech

2021 Forum, [S.L.], p. 1-26, January 4th, 2021. American Institute of Aeronautics and Astronautics. http://dx.doi.org/10.2514/6.2021-1298.

[21] STOLL, A. M., BEVIRT, J., MOORE, M. D., FREDERICKS, W. J., and BORER, N. K.. **Drag Reduction Through Distributed Electric Propulsion**. 14th AIAA Aviation Technology, Integration, and Operations Conference, AIAA Paper 2014-2851, June, 2014. https://doi.org/10.2514/6.2014-2851.

[22] VARGES, Paulo Henrique Caires Rocha. **Estudo conceitual de um eVTOL para transporte urbano em massa**. 2018. 91 f. TCC (Bachelor Degree) – Aerospace Engineer, Universidade Federal de Minas Gerais, Belo Horizonte, 2018.

[23] **VA-X4**. Available at: https://vertical-aerospace.com/va-x4/. Access on July 26th, 2021.

[24] **Volocity**. Available at: https://www.volocopter.com/solutions/volocity. Access on August 2nd, 2021.

[25] WASSERMAN, Shawn. **Choosing the Right Turbulence Model for Your CFD Simulation:** Turbulence model definitions, strengths, weaknesses and best practices for your CFD simulation. 2016. Available at: https://www.engineering.com/story/choosing-the-right-turbulence-model-for-your-cfd-simulation. Access on October 15th, 2021.

[26] **Wisk Cora.** Available at: https://wisk.aero/aircraft/. Access on August 2nd, 2021.

APPENDIX I

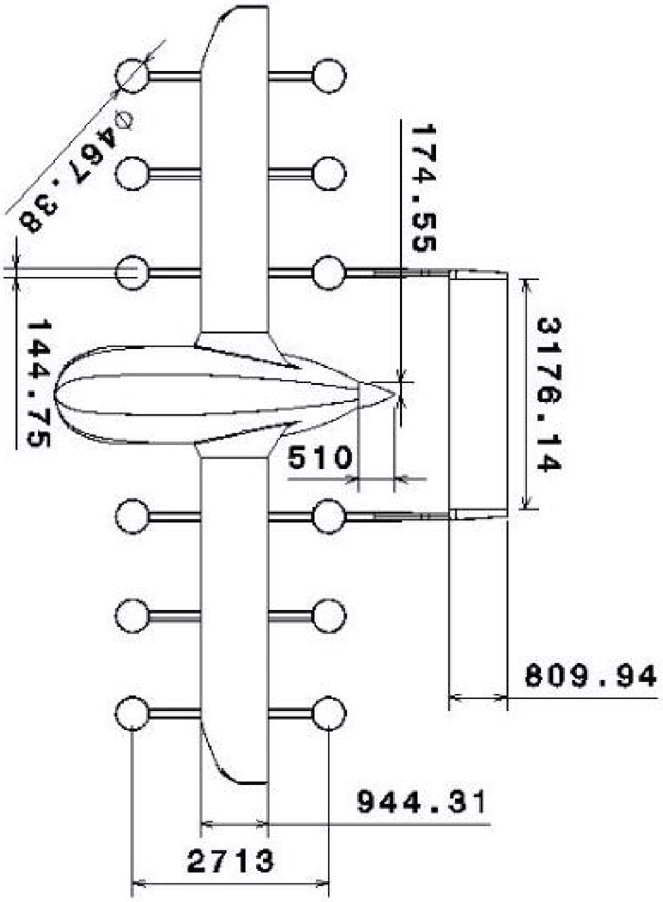
⌀467.38
174.55
144.75
3176.14
510
809.94
944.31
2713

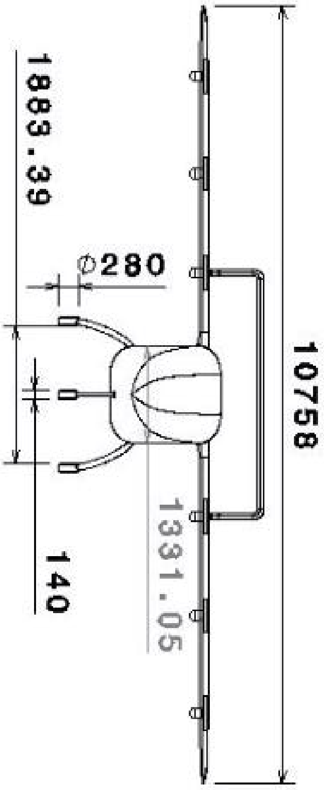
1883.39
⌀280
10758
140
1331.05

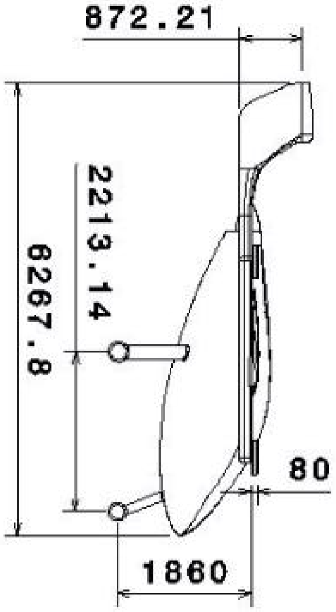
872.21
2213.14
8267.8
80
1860